

1 **Three-Dimensional Variational Multi-Doppler Wind Retrieval over complex**  
2 **terrain**

3 Ting-Yu Cha and Michael M. Bell

4 <sup>a</sup> *National Center for Atmospheric Research, Boulder, CO, United States*

5 <sup>b</sup> *Department of Atmospheric Science, Colorado State University, Fort Collins, Colorado, United*  
6 *States*

7 *Corresponding author: Ting-Yu Cha, tycha@ucar.edu*

8 ABSTRACT: The interaction of airflow with complex terrain has the potential to significantly  
9 amplify extreme precipitation events and modify the structure and intensity of precipitating cloud  
10 systems. However, understanding and forecasting such events is challenging, in part due to the  
11 scarcity of direct in-situ measurements. Doppler radar can provide the capability to monitor extreme  
12 rainfall events over land, but our understanding of airflow modulated by orographic interactions  
13 remains limited. The SAMURAI software is a three-dimensional variational (3DVAR) technique  
14 that uses the finite element approach to retrieve kinematic and thermodynamic fields. The analysis  
15 has high fidelity to observations when retrieving flows over a flat surface, but the capability of  
16 imposing topography as a boundary constraint is not previously implemented. Here we imple-  
17 ment the immersed boundary method (IBM) as pseudo-observations at their native coordinates in  
18 SAMURAI to represent the topographic forcing and surface impermeability. In this technique,  
19 neither data interpolation onto a Cartesian grid nor explicit physical constraint integration during  
20 the cost function minimization is needed. Furthermore, the physical constraints are treated as  
21 pseudo-observations, offering the flexibility to adjust the strength of the boundary condition. A  
22 series of observing simulation sensitivity experiments (OSSEs) using a full-physics model and  
23 radar emulator simulating rainfall from Typhoon Chanthu (2021) over Taiwan are conducted to  
24 evaluate the retrieval accuracy and parameter settings. The OSSE results show that the strength of  
25 the IBM constraints can impact the overall wind retrievals. Analysis from real radar observations  
26 further demonstrates that the improved retrieval technique can advance scientific analyses for the  
27 underlying dynamics of orographic precipitation using radar observations.

## 28 **1. Introduction**

29 The vertical transport of water vapor and air are crucial in the weather and climate system,  
30 yet vertical motion ( $w$ ) remains one of the most challenging wind components to observe and  
31 predict accurately. In complex terrain, orographically-induced airflow plays a significant role in  
32 modulating weather systems, impacting precipitation intensity and cloud structure. The interaction  
33 between clouds and topography involves various physical mechanisms that can lead to extreme  
34 rainfall and intense convective storms (Zipser et al. 2006; Chien and Kuo 2011; Houze 2012).

35 Doppler radar observations present an opportunity to understand the airflow associated with  
36 orographic interactions and the key ingredients that impact the intensity and duration of severe  
37 weather. Multiple-Doppler radar observations can be used to reconstruct a full three-dimensional  
38 wind field (Ray et al. 1979), but the accuracy of  $w$  remains challenging, especially when the  
39 precipitating system is over a mountainous area (del Moral et al. 2020). Most state-of-the-  
40 art radar synthesis software currently incorporates the mass continuity equation to retrieve  $w$   
41 throughout the atmospheric column. The mass continuity equation enforces the mass-weighted  
42 vertical flow to be physically consistent with the divergence of the mass-weighted horizontal  
43 flow. However, additional boundary conditions are necessary to impose physical constraints on  
44 airflow movement over terrain. Accurate representation of the boundary conditions is required  
45 to retrieve a reasonable three-dimensional wind field and to further study storm dynamics. In  
46 this study, we implement boundary conditions at the terrain height to represent the topographic  
47 forcing and surface impermeability in the three-dimensional variational data assimilation (3DVAR)  
48 multi-Doppler radar software for recovering the wind field over complex terrain.

49 Variational techniques have been widely used for multi-Doppler retrievals (Gamache et al. 1995;  
50 Gao et al. 1999, 2004; Potvin et al. 2012b; Bell et al. 2012; North et al. 2017). The 3DVAR approach  
51 solves for the optimal wind field by minimizing a cost function that incorporates various types of  
52 observations with specified uncertainties and the algorithm assumptions (e.g. mass continuity  
53 equation). Different sources of uncertainties include algorithm effects, instrument effects, and  
54 sampling effects. Algorithm effects include the interpolation and smoothing techniques used to map  
55 the radar polar grid to a common Cartesian coordinate system (Collis et al. 2010), hydrometeor fall  
56 speed estimates (Steiner 1991), and other algorithm assumptions (e.g. mass continuity integration,  
57 Matejka and Bartels (1998)). Hildebrand et al. (1994) shows that instrument effects can contribute

58 to errors of up to  $1 \text{ m s}^{-1}$  in Doppler wind measurements due to radar processor design and  
59 measurement techniques. Sampling effects include data spacing and density, which are impacted  
60 by the geometry of dual or multi-radar beams and beam blockage by terrain, as well as the temporal  
61 evolution of weather phenomena, and data collection time span (Hildebrand and Mueller 1985;  
62 Oue et al. 2019; Cha and Bell 2021). In Oue et al. (2019), a radar emulator was used to investigate  
63 the quality of vertical wind retrieval in relation to observational error sources. Their findings  
64 demonstrate that the choice of volume coverage pattern (VCP) elevation strategy and sampling  
65 time can significantly influence the accuracy of retrieved vertical velocity. Additionally, utilizing  
66 rapid-scan radars to reduce the data collection period can greatly enhance the quality of the results.  
67 Understanding and accounting for these uncertainties are crucial for accurate wind retrieval in the  
68 3DVAR approach.

69 Most 3DVAR approaches have been developed for retrievals over flat surfaces, but retrievals over  
70 complex terrain require additional considerations of the topographic forcing and impermeability  
71 at the terrain height. Georgis et al. (2000) was one of the first studies that developed a variational  
72 approach to account for orographic effects in multi-Doppler radar analysis. In their approach, a first  
73 guess of the vertical velocity is derived through the integration of the mass continuity equation.  
74 The vertical wind is then iteratively solved until a converged solution is obtained. Chong and  
75 Cosma (2000) improved the variational MULTiple-Doppler Synthesis and Continuity Adjustment  
76 Technique (MUSCAT; Bousquet and Chong (1998)) by implementing the capability to retrieve wind  
77 field over complex terrain. Chong et al. (2000) further integrated the aforementioned approaches  
78 and presented an improved multiple-Doppler analysis method for real-time recovery of the wind  
79 field over mountainous regions, and a low-pass filter is used to partially recover the wind flow  
80 along the radar baseline. Employing a low-pass filter helps alleviate retrieval instabilities in areas  
81 with sparse data coverage and along the radar baseline.

82 Liou and Chang (2009) developed a variational multiple-Doppler radar three-dimensional wind  
83 synthesis method over flat terrain. The accuracy of vertical velocity retrieval was improved by  
84 incorporating the vertical vorticity equation and removing the assumption of prescribed vertical  
85 velocities at the data boundary. Building upon this work, Liou et al. (2012) further advanced  
86 the technique by introducing the immersed boundary method (IBM) with a ghost cell approach.  
87 This method allows for the recovery of the wind field above the terrain while considering the

88 topographic forcing (Tseng and Ferziger 2003). The IBM approach provides realistic topographic  
89 forcing within a standard Cartesian grid, eliminating the need to convert to a terrain-following  
90 coordinate system. This capability allows for accurate representation of the topographic effects  
91 without the requirement of transforming the coordinate system.

92 The Spline Analysis at Mesoscale Utilizing Radar and Aircraft Instrumentation (SAMURAI)  
93 analysis technique employs a finite element approach using a series of overlapping cubic B-  
94 spline basis functions. This approach offers several advantages over a conventional grid-point  
95 representation (Bell et al. 2012; Foerster et al. 2014), including:

- 96 • The use of a finite element representation for functions allows for a scale-controlled analysis  
97 that can incorporate multiple spatial filters in the background error covariance and analytic  
98 spatial derivatives in observational space, eliminating the need of adding terms to the cost  
99 function to account for additional constraints. This feature enables the user to easily select the  
100 desired scales and constraints for an analysis.
- 101 • Traditional 3DVAR multi-Doppler approaches typically involve the interpolation of polar radar  
102 data to a Cartesian coordinate system, which has been shown can introduce artifacts in vertical  
103 velocities (Collis et al. 2010). In SAMURAI, the finite element method can handle irregular  
104 data distributions and complex immersed boundary geometries directly without interpolation  
105 to a Cartesian grid. Instead, the data can be used in the variational minimization in their native  
106 locations. This feature reduces one of the potential interpolation errors in the analysis.
- 107 • Spatial derivative constraints can be obtained from physical equations, such as the mass  
108 continuity equation and/or the momentum equations (Foerster et al. 2014). The finite element  
109 formulation allows for the specification of these derivative constraints as pseudo-observations  
110 at any point in their native coordinate. Physical constraints on the spatial gradients can be  
111 treated as pseudo-observations at any given point with specified pseudo-observational errors  
112 that are implicitly integrated during the cost function minimization rather than explicitly  
113 integrated.

114 The SAMURAI technique has demonstrated its ability to generate high-quality scientific results  
115 over flat surfaces, as evidenced by previous studies (Bell et al. 2012; Foerster et al. 2014; Martinez  
116 et al. 2019; Cha et al. 2020). However, when it comes to retrievals over complex terrain, additional

117 assumptions regarding terrain boundaries need to be considered. The current study improves the  
118 SAMURAI technique by incorporating retrieval capabilities over complex terrain. We implement  
119 the IBM method as pseudo-observations which allows for the boundary conditions at any specified  
120 terrain height with adjustable pseudo-observational errors. The analytic nature of spatial derivatives  
121 eliminates the requirement for the ghost cell approach utilized in finite difference methods. The  
122 outline of the paper is as follows: Section 2 describes the details and the formulation of the 3DVAR  
123 approach designed for over complex terrain. Section 3 presents the dataset used and outlines the  
124 experimental setup to assess the accuracy of the immersed boundary solver. Observing System  
125 Simulation Experiments (OSSEs) are conducted using simulated data from Typhoon Chanthu  
126 (2021) which produced heavy rainfall over complex topography in northern Taiwan. Section 4  
127 investigates the performance of the newly developed method through sensitivity tests on various  
128 experimental setups, including: a) varying the strength of terrain forcing constraint at the boundary,  
129 b) exploring the resolution and details of complex terrain slope, c) assessing the contribution of  
130 vertical wind retrieval from mass continuity and terrain forcing, and d) analyzing the impact of  
131 grid spacing and Gaussian recursive filter settings. Section 5 demonstrates the applicability of the  
132 wind retrieval over complex terrain using real radar data from Typhoon Chanthu (2021). Section  
133 6 provides a summary of the findings and discusses their implications.

## 134 **2. Methodology**

### 135 *a. SAMURAI*

136 SAMURAI uses a set of cubic B-spline basis functions that are continuous and differentiable  
137 up to the third-order derivative. Combining a set of spline functions allows for the formation  
138 of the shape of any function while still being differentiable. The use of spline basis functions  
139 in representing the atmospheric structure allows for the specification of pseudo-observations of  
140 spatial gradients.

141 The nodal spacing in SAMURAI determines the minimum feature size that can be resolved  
142 by the function. The finite element approach in SAMURAI provides flexibility in specifying  
143 nodal spacing and spatial gradients at any point and space, which allows for a more adaptable  
144 representation of the atmospheric structure. These pseudo-observations of spatial gradients are  
145 integrated during the cost function minimization, along with the observations and background.

146 The cost function, formulated as an incremental form, incorporates weights based on observations,  
147 observation errors, background state estimates, and background state errors. The cost function is  
148 minimized at the most likely atmospheric state at the analysis time based on the input data and  
149 specified errors. SAMURAI initially employed a nonlinear Conjugate Gradient (NCG) method,  
150 which involved computationally intensive tasks such as evaluating the gradient and performing a  
151 line search in each iteration until convergence (Gao et al. 2004). Dennis et al. (2022) improved the  
152 optimization solver performance by implementing a Truncated Newton (TN) solver, optimizing  
153 code, and porting SAMURAI to GPU environments, which results in a substantial reduction in the  
154 overall execution time. The combined improvement efforts have resulted in speed improvements  
155 exceeding 100 times compared to the original SAMURAI code. For more detailed information  
156 regarding these improvements, please refer to Dennis et al. (2022).

157 SAMURAI has three spatial filters to facilitate analysis smoothing and the propagation of infor-  
158 mation from observations throughout the domain, including the Fourier spectral filter, the spline  
159 cutoff, and the Gaussian recursive filter. The Fourier spectral filter is mainly used for removing  
160 high-wavenumber features directly in the spectral domain or restricting to a mean value along a  
161 particular axis (i.e. wavenumber zero only). The spline cutoff is implemented as a third derivative  
162 constraint on the cubic B-spline basis during the spline transform (Ooyama 2002). The Gaussian  
163 recursive filter operates as a Gaussian low-pass filter utilizing an efficient recursive operator (Purser  
164 et al. 2003). Smaller filter lengths retain more detail, albeit with a potential to capture noise, while  
165 larger filter lengths yield greater smoothing but may result in the loss of fine details. These filters  
166 can be used individually or in combination to produce different responses. Choosing an appropri-  
167 ate filter type and length based on the data distribution is crucial in obtaining the desired physical  
168 scales of interest in the analysis.

169 In this study, we utilized a combination of the spline-cutoff filter with 2 nodes in the horizontal  
170 direction and the Gaussian recursive filter with 4 nodes in the horizontal and 2 nodes in the vertical  
171 direction. The sensitivity of the Gaussian recursive filter setting will be investigated in Section 4,  
172 while the sensitivity of the Fourier filter and spline cutoff setting will not be addressed in this study.

173 *b. The immersed boundary method*

174 Urban and mountainous environments often feature steep slopes and complex geometries. The  
 175 IBM method enables flows in such complex terrains to be simulated at their native spacing, without  
 176 the need to conform to a specific coordinate system. This approach preserves the topography with  
 177 high-order boundary representations, accurately capturing the intricate features of the terrain. This  
 178 ensures that winds influenced by terrain forcing can be realistically resolved.

179 The IBM has been implemented into the Weather Research and Forecasting (WRF) model  
 180 (Lundquist et al. 2010), and an observational wind retrieval technique Wind Synthesis System  
 181 using Doppler Measurements (WISDDOM, Liou et al. (2012)). Previous studies have adopted a  
 182 finite-difference approach, where the body force term is applied to ghost cells located within the  
 183 terrain. This ghost cell method is able to handle rigid boundaries and produce a sharp representation  
 184 of the fluid solid interface. In SAMURAI, the ghost cell approach can be circumvented through two  
 185 main implementations. First, the finite element approach is utilized, allowing the terrain boundary  
 186 nodes to be positioned independently of specific computational nodes. This flexibility enables the  
 187 boundary spatial derivatives to be computed at their original locations. Second, SAMURAI uses  
 188 a set of overlapping cubic B-splines that are differentiable up to the third-order derivative (Fig. 1).  
 189 This allows the boundary condition to be applied directly at the terrain height instead of using a  
 190 traditional ghost cell.

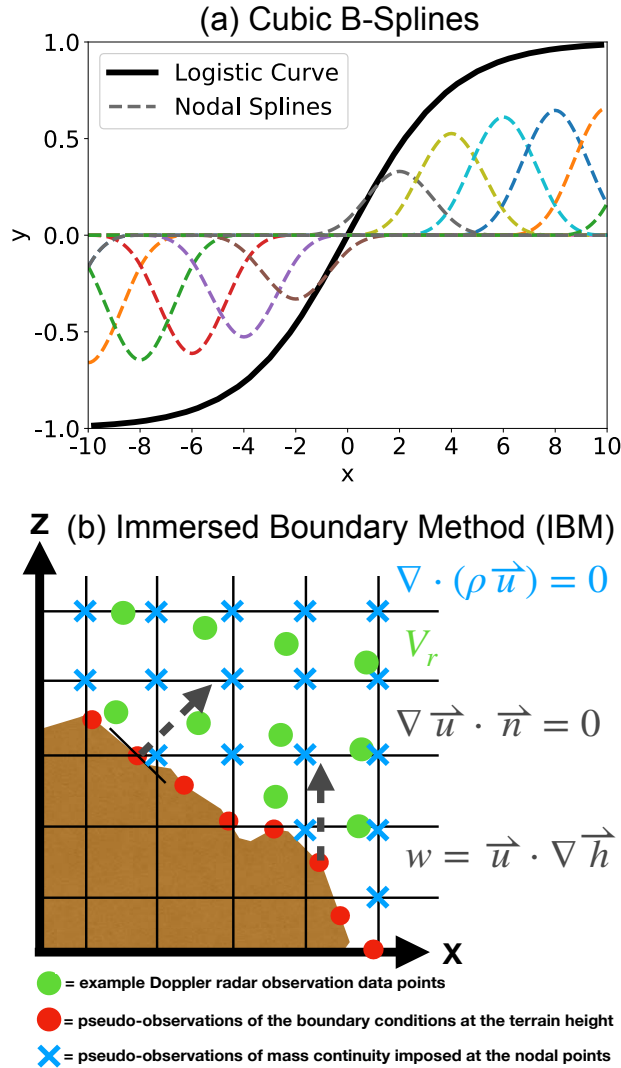
197 Two boundary conditions are implemented into SAMURAI, following Liou et al. (2012)'s  
 198 method:

$$\frac{\partial u}{\partial n} = 0 = \nabla \mathbf{u} \cdot \mathbf{n} = \frac{-\left(\frac{\partial h}{\partial x}\right)}{\sqrt{1 + \left(\frac{\partial h}{\partial x}\right)^2 + \left(\frac{\partial h}{\partial y}\right)^2}} \frac{\partial u}{\partial x} + \frac{-\left(\frac{\partial h}{\partial y}\right)}{\sqrt{1 + \left(\frac{\partial h}{\partial x}\right)^2 + \left(\frac{\partial h}{\partial y}\right)^2}} \frac{\partial u}{\partial y} + \frac{1}{\sqrt{1 + \left(\frac{\partial h}{\partial x}\right)^2 + \left(\frac{\partial h}{\partial y}\right)^2}} \frac{\partial u}{\partial z} \quad (1)$$

$$\frac{\partial v}{\partial n} = 0 = \nabla \mathbf{v} \cdot \mathbf{n} = \frac{-\left(\frac{\partial h}{\partial x}\right)}{\sqrt{1 + \left(\frac{\partial h}{\partial x}\right)^2 + \left(\frac{\partial h}{\partial y}\right)^2}} \frac{\partial v}{\partial x} + \frac{-\left(\frac{\partial h}{\partial y}\right)}{\sqrt{1 + \left(\frac{\partial h}{\partial x}\right)^2 + \left(\frac{\partial h}{\partial y}\right)^2}} \frac{\partial v}{\partial y} + \frac{1}{\sqrt{1 + \left(\frac{\partial h}{\partial x}\right)^2 + \left(\frac{\partial h}{\partial y}\right)^2}} \frac{\partial v}{\partial z}$$

$$w = u \frac{\partial h}{\partial x} + v \frac{\partial h}{\partial y} \quad (2)$$





191 FIG. 1. (a) An example function and its component b-spline amplitudes. The thick black line is a logistic  
 192 curve, and the dashed colored lines represent each individual b-spline at the nodal points that sum to represent  
 193 the function. (b) A diagram illustrating the observational data points (green dots), pseudo-observations obtained  
 194 from the two terrain boundary conditions (red dots and dashed lines), and pseudo-observations obtained from  
 195 the mass continuity equation (blue cross). The background mesh gridlines represent the output analysis grid  
 196 spacing.

199 where  $n$  is the unit vector perpendicular to the boundary,  $u$  is the zonal wind,  $v$  is the meridional  
 200 wind,  $w$  is the vertical wind, and  $h$  denotes the terrain height. The Neumann boundary condition  
 201 is applied to  $u$  and  $v$  (Eq. 1), while the Dirichlet boundary condition is used for  $w$  (Eq. 2). The  
 202 Neumann boundary ensures that the total mass flux across the boundary is set to zero, preventing

203 mass flux from penetrating the terrain. The Dirichlet boundary ensures that the vertical velocity  
204 at the terrain height is determined by the horizontal wind components  $u$  and  $v$ , thus accounting for  
205 the influence of topographic forcing. Given the correlation between the induced vertical velocity  
206 by topographic forcing and the terrain slope, the selection of an appropriate terrain map becomes  
207 crucial for resolving the desired scale of interest. This aspect will be further explored in Section 4.

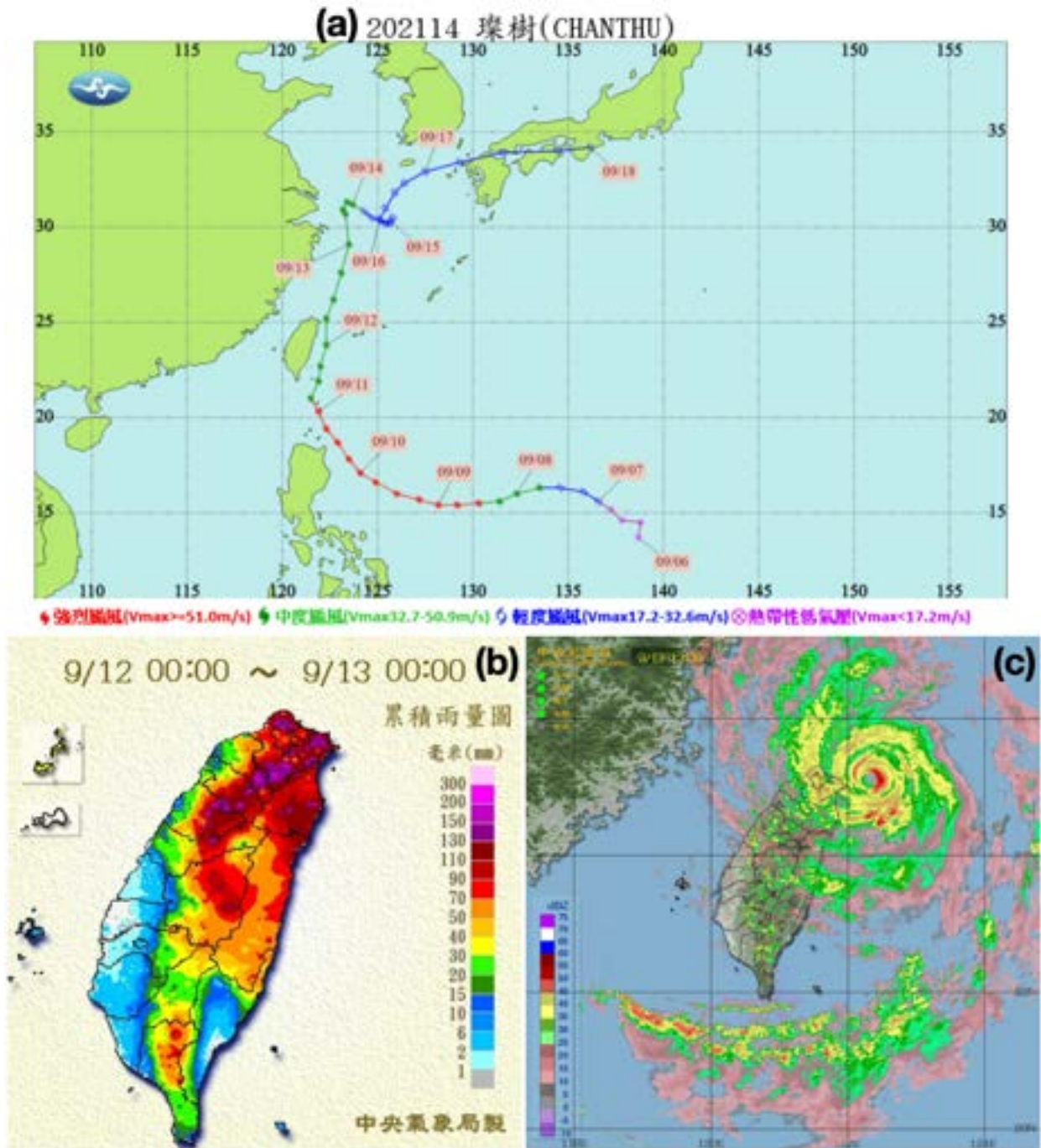
### 208 **3. Data and Sensitivity experimental setup**

#### 209 *a. Typhoon Chanthu (2021)*

210 Figure 2a depicts the track and intensity of Typhoon Chanthu. According to the Japan Mete-  
211 orological Agency (JMA), the maximum wind speed of Chanthu was recorded as 115 kt (59 m  
212  $s^{-1}$ ) when the typhoon was located northeast of Luzon. Despite undergoing a weakening trend  
213 after reaching its peak intensity, Typhoon Chanthu exhibited intense eyewall convection over 50  
214 dBZ as indicated by the radar composite reflectivity at 05:30 UTC on 12 September (Fig. 2c).  
215 The accompanying rainband, characterized by reflectivity values of 35-40 dBZ, made landfall in  
216 northern Taiwan. The spiral rainband exhibited a predominantly perpendicular orientation to the  
217 mountain slope, resulting in enhanced rainfall parallel to the ridge. Figure 2b shows the 24-h  
218 rainfall accumulation from 08 UTC 12 September to 08 UTC 13 September. A distinct band of  
219 enhanced precipitation, with a maximum accumulation exceeding 200 mm, is observed parallel to  
220 the snow mountain ridge. Interestingly, the minimum rainfall recorded over the Central mountain  
221 ranges from 20 to 30 mm. These variations in rainfall accumulation and patterns suggest that  
222 topography plays a significant role in influencing the amount of precipitation, in addition to the  
223 influence of the typhoon circulation. The widespread orographic precipitation and strong wind  
224 speeds were captured by the Wufenshen (RCWF) and Shulin (RCSL) radar observations under an  
225 adequate dual Doppler geometry (Table 2). Therefore, Typhoon Chanthu is selected as the case  
226 study for testing the improved technique.

#### 231 *b. Dataset*

232 An OSSE is conducted for Typhoon Chanthu on 12 September 2021 when the typhoon's rainband  
233 made landfall in northern Taiwan, resulting in rainfall exceeding 50 mm within an hour in the  
234 mountainous region. OSSE studies are typically carried out to evaluate the effects of operational



227 FIG. 2. (a) Typhoon Chanthu's track and intensity. (b) 24-h rainfall accumulation from 08 UTC 12 September  
 228 to 08 UTC 13 September. Time shown in the plot is in LST. (c) The composite radar reflectivity at 0530  
 229 UTC 12 September. All the figures were derived from the Central Weather Bureau Typhoon Database ([https://rdc28.cwb.gov.tw/TDB/public/typhoon\\_detail?typhoon\\_id=202114](https://rdc28.cwb.gov.tw/TDB/public/typhoon_detail?typhoon_id=202114)).  
 230

235 observing systems on observation-based value-added products and weather forecasts. The WRF  
236 simulation provides kinematic and thermodynamic variables with a physical understanding of the  
237 orographic effects on precipitating clouds and wind flow.

238 The WRF simulation uses version 4.1.3 (Skamarock et al. 2021). The Morrison double-moment  
239 scheme was utilized (Morrison et al. 2005). The MYNN2.5 (Mellor-Yamada-Nakanishi-Niino  
240 level 2.5) PBL scheme was adopted (NAKANISHI and NIINO 2009). The domains are configured  
241 as fixed triple-nested domains with two-way interaction for the second and third domains. The  
242 outermost domain has a horizontal grid spacing of 9 km, the second domain has a spacing of 3  
243 km, and the innermost domain has a resolution of 1 km. The innermost domain has a horizontal  
244 grid spacing of 1 km and 51  $\sigma$ -layers in the vertical. The initialization of this domain is based  
245 on the boundary conditions provided by the 3-km simulation. The WRF terrain height data has  
246 a horizontal resolution of 30-arc seconds, which corresponds to approximately 1 km horizontally.  
247 The terrain data is available at each grid point and has an averaged slope of  $6 \times 10^{-2}$  ( $\nabla h$ , unitless).  
248 In the WRF simulation, the native output is in the pseudo-pressure coordinate, resulting in a vertical  
249 grid that is stretched in physical space. The minimum vertical grid spacing in the WRF grid is  
250 approximately  $\Delta z_{min} \approx 23.22$  m, which is found at the peak of the hill. On the other hand, the  
251 maximum vertical grid spacing is approximately 644.46 m, occurring at a height of approximately  
252  $z \approx 5.2$  km.

253 The 1-km simulation was initialized following a 3-hour run of the first and second domains,  
254 and output was produced at 15-minute intervals. The innermost domain is designed to cover  
255 the northern part of Taiwan during the interaction of Typhoon Chanthu's rainband with the local  
256 topography. The simulation output at 05:30:02 UTC on September 12 is selected as the input  
257 data for the subsequent datasets described. As the focus of this study is on the impact of complex  
258 terrain on wind retrieval, the sampling time for the radar volume coverage pattern (VCP) and storm  
259 evolution are not considered.

260 Three types of OSSE datasets were generated:

#### 261 1) REFERENCE ("TRUTH")

262 The WRF simulation is on a sigma coordinate, and the filtering length and actual resolving scale  
263 may slightly differ from the SAMURAI analysis. To ensure an equitable comparison, the sigma-

264 level output data of the innermost WRF domain at 05:30:02 UTC 12 September snapshot was  
265 loaded into SAMURAI. The reference analysis was generated by ingesting known data at WRF  
266 native coordinates with an observational error of 1 (unit corresponding to the variables), including  
267 a three-dimensional wind field ( $u$ ,  $v$ ,  $w$ ), temperature, water vapor mixing ratio, dry air density,  
268 moist air density, and reflectivity. The terrain boundary error was set at  $1 \times 10^{-3}$  (unitless) for the  
269 analysis, as shown in the first column of Table 1.

## 270 2) CR-SIM

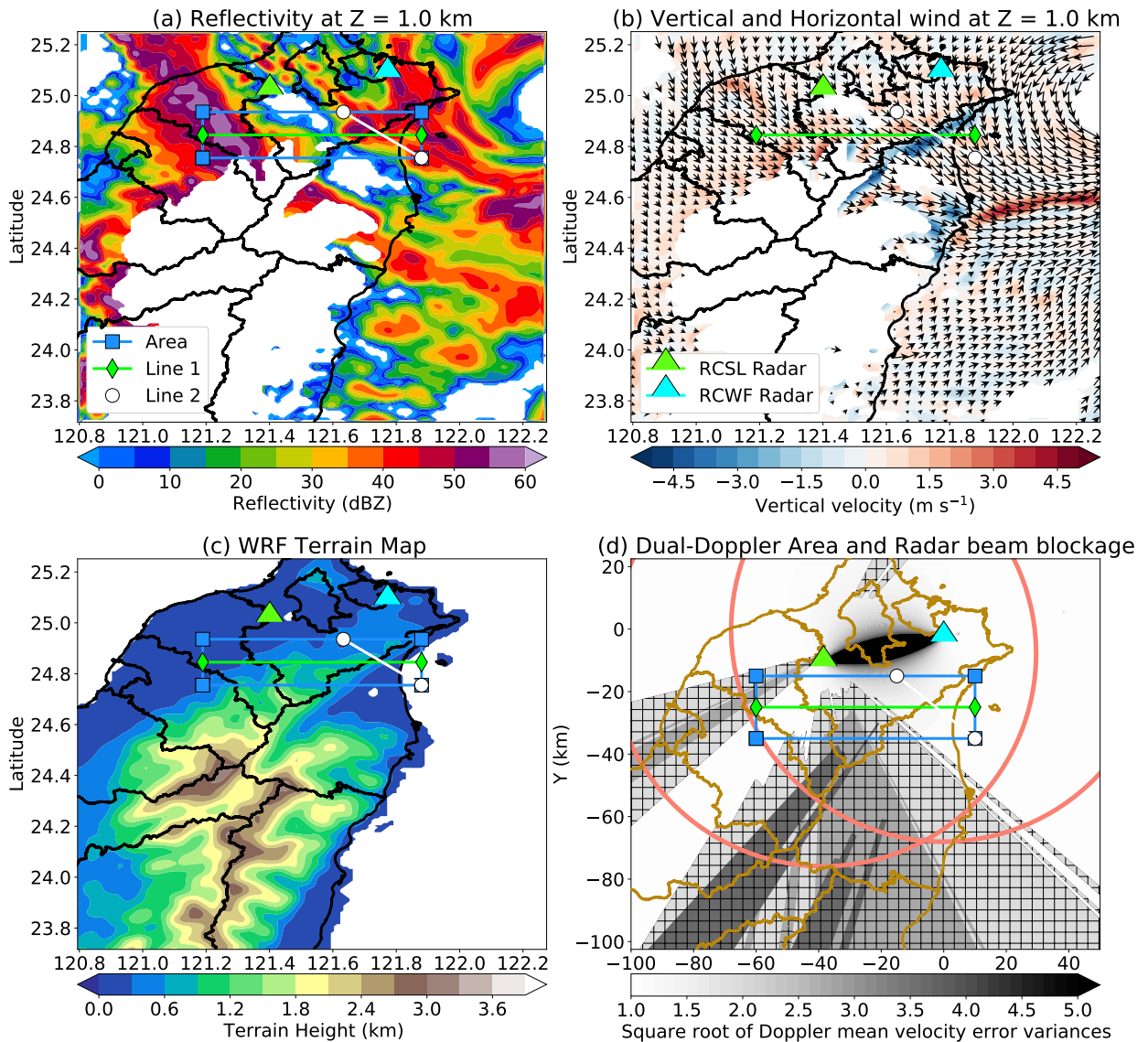
271 The Cloud resolving Model Radar SIMulator (CR-SIM, Oue et al. (2020)) utilized the WRF  
272 simulation as input to generate equivalent radar reflectivity factor ( $Z_{hh}$ ) and Doppler velocity ( $V_d$ )  
273 at the model grid. CR-SIM is a radar simulator designed to replicate multi-wavelength, zenith-  
274 pointing, and scanning radar observations based on high-resolution cloud-resolving models. By  
275 employing the same microphysics scheme, CR-SIM can transform model variables into radar and  
276 lidar observables, facilitating direct comparisons between numerical weather model output and  
277 radar observations. The simulated radar observables account for sampling strategies, enabling  
278 the assessment of errors arising from sampling and uncertainties associated with multi-Doppler  
279 wind retrievals. This dataset at WRF model grid was generated by using the VCPs of the RCWF  
280 and RCSL radars, without considering time evolution (Table 2). The purpose of evaluating this  
281 dataset against the truth is to investigate Doppler errors in scenarios lacking direct vertical wind  
282 observations.

## 283 3) RADAR-FILTER

284 The third dataset was generated by transforming the second dataset from the WRF model grid to  
285 radar polar coordinates. This dataset, which incorporates more realistic radar characteristics, is  
286 evaluated against the first and second datasets to investigate radar geometry and sampling errors.

292 One caveat to note is that none of the datasets described above account for the beam blockage  
293 effect, which should be addressed in future work.

304 Figure 3 shows the “true” fields of reflectivity and vertical velocity, which are used to demonstrate  
305 the retrieval performance for the sensitivity tests. The white area in the horizontal cross-section at  
306 1 km (Fig. 3a and b) is a result of the terrain (Fig. 3c). To ensure an objective selection of an area  
307 of interest with suitable radar beam geometry and appropriate spatial resolution, the dual-Doppler



294 FIG. 3. Horizontal cross sections of (a) reflectivity and (b) vertical (shading) and horizontal wind (vectors)  
 295 at 1 km altitude from the “truth”. (c) WRF terrain map. (d) The effective dual-Doppler radar lobes. Large  
 296 red circles represent the maximum observing range of RCSL and RCWF, respectively. The shading between  
 297 the radar radars denotes the Doppler mean velocity error variances of the two radars, which are determined by  
 298 the dual Doppler radar beam geometry. The light gray contour with black hatches represents the RCSL radar  
 299 beam blockage at the lowest elevation angle ( $1^\circ$ ), while the dark gray contour with black hatches represents the  
 300 second lowest PPI ( $2^\circ$ ). The darkest gray contour with black hatches indicates the RCWF radar beam blockage  
 301 at the lowest elevation angle ( $0.483^\circ$ ). The triangles denote the RCSL (green) and RCWF (cyan) radar locations  
 302 respectively. The blue box denotes the area where the accuracy of retrieval is assessed. The green and white line  
 303 denotes two vertical cross sections that will be shown in Section 4

287 TABLE 1. Sensitivity experimental setups designed to assess the performance of various configurations,  
 288 including terrain boundary constraint, Doppler sampling limitations, and slope of terrain map. Note that the  
 289 scientific notation of 1E-3 represents  $1 \times 10^{-3}$ , 6E-2 represents  $6 \times 10^{-2}$ , and so on. NE and DE stand for the  
 290 pseudo-observation errors due to the Neumann boundary and Dirichlet boundary, respectively. The notation  $i$   
 291 and  $j$  represent the power of the exponents used with a base of 10.

Setup/Labels	Reference (“Truth”)	CR-SIM: NE $i$ DE $j$	Radar-Filter: NE $i$ DE $j$	Radar-Filter: S $k$
Data coordinates	WRF model grid ( $x, y, \sigma$ )	WRF model grid ( $x, y, \sigma$ )	Radar grid (azi, elev, range)	Radar grid (azi, elev, range)
Input data	$u, v, w, T,$ $q_v, \rho_a, \rho_m, Z_{hh}$	$Z_{hh}, V_d$	$Z_{hh}, V_d$	$Z_{hh}, V_d$
Neumann Error ( $i$ ) $i$ in [0,1,2,3] (unitless)	1E-3	1E-3, 1E-2, 1E-1, 1E-0	1E-3, 1E-2, 1E-1, 1E-0	1E-3, 1E-2, 1E-1, 1E-0
Dirichlet Error ( $j$ ) $j$ in [0,1,2,3] (unitless)	1E-3	1E-3, 1E-2, 1E-1, 1E-0	1E-3, 1E-2, 1E-1, 1E-0	1E-3, 1E-2, 1E-1, 1E-0
Mean slope ( $k$ ) (unitless)	6E-2	6E-2	6E-2	6E-2, 8E-2, 1E-1
# of experiment	1	4×4	4×4	3×4×4

308 lobes are depicted in Fig. 3d. Additionally, an accurate retrieval of the vertical velocity relies  
 309 heavily on the dual-Doppler measurements, the mass continuity equation, and the assumed terrain  
 310 boundary conditions. Therefore, selecting an effective area for dual-Doppler measurements is  
 311 crucial in order to minimize errors caused by Doppler geometry, which ensures that the algorithm  
 312 assumptions regarding the terrain boundary conditions can be evaluated with fewer concerns about  
 313 other factors. An effective dual-Doppler measurement area is primarily determined by three factors:  
 314 the minimum spatial resolution required to accurately resolve the phenomenon of the interest, the  
 315 maximum acceptable error in horizontal velocity, and the distance between the radars. Increasing  
 316 the radar separation distance can enhance the accuracy of the two velocity components over a larger  
 317 area, but it can lead to a degradation in spatial resolution near the radar locations. The dual Doppler  
 318 lobes can be defined by the intersection of the acceptable velocity error variance, and the maximum  
 319 of the desired spatial resolution (Davies-Jones 1979; Friedrich and Hagen 2004). The maximum  
 320 spatial resolution is determined by the radar separation distance and a selected cross-beam angle.  
 321 In our case, the distance between the RCSL and RCWF is 39.26 km, yielding a fine resolution at  
 322 close range. The beam crossing angle ( $\beta$ ) is chosen to be  $35^\circ$  so that the resolution of the resulting

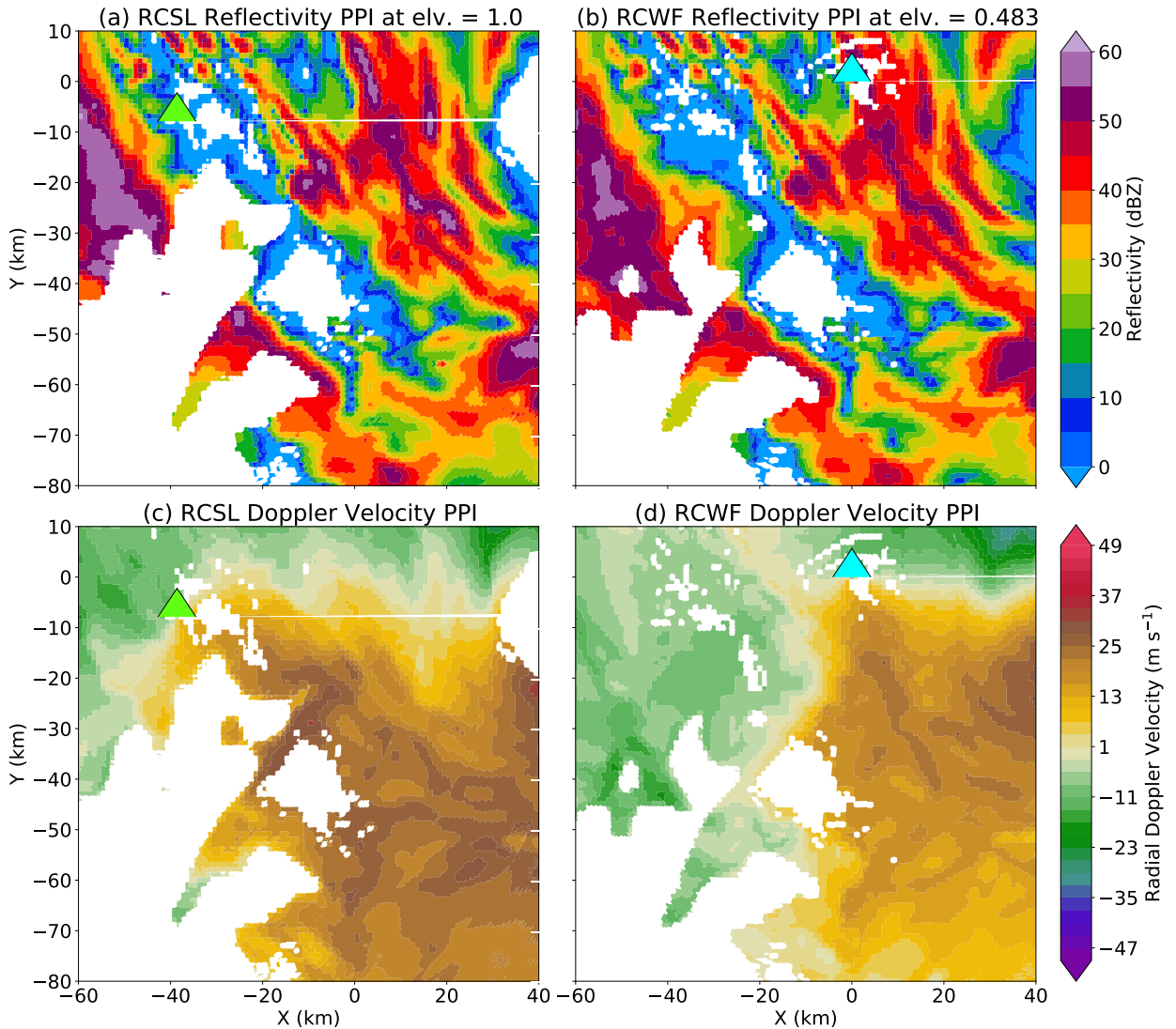
merged data is  $\approx 1$  km. The horizontal wind solution is obtained by a geometrically weighted sum of the interpolated radial velocities. As the radial velocity measurements are sampled independently by different radars, the individual Doppler velocity variance can be used to estimate the error in the wind synthesis due to the geometry. The square root of the mean Doppler velocity variance derived from the two radars can be calculated to determine the potential error in the wind solution. In addition, partial or total beam blockage caused by mountains may limit the measurements from the low-elevation angles. Figure 3d's contours show the low-elevation beams where they are blocked by the surrounding terrain. Taking into account these factors, the resulting area for dual-Doppler analysis and selected cross sections with minimal beam blockage are shown in Fig. 3d.

To conduct realistic testing using the Taiwanese radar operational network and assess the overall wind retrieval for Section 5 with real radar observations, we use the RCWF and RCSL radar configuration for the simulated radar measurements (Table 2). Note that in the following Section 4, the results assume a static model output, where the radars collect data instantaneously based on their VCPs without any temporal evolution. All radar gate data points are at the same time step to reduce the uncertainty in retrieved winds caused by time discrepancies. Plan position indicator (PPI) of simulated reflectivity and Doppler velocity observed by the RCSL and RCWF are shown in Fig. 4 as an example.

TABLE 2. The configuration of the RCWF and RCSL radars.

Radar	RCWF	RCSL
Radar location	(25.071182N, 121.781205E)	(25.00N, 121.4E)
Radar height (m)	765	298
Radar frequency (GHz)	3.0 (S band)	5.5 (C band)
Beamwidth	0.89	0.92
Range resolution (m)	250.0	250.0
Elevation angle	0.4833984, 0.8789062, 1.318359, 1.801758, 2.416992, 3.120117, 3.999023, 5.097656, 6.416016, 7.998047, 10.01953, 11.99707, 14.01855, 16.69922, 19.51172	1, 2, 3, 4, 5, 6, 9.9, 14.6, 19.5, 24.5, 29.9
Time period (OSSEs)	Simulation output at 05:30:02 UTC	
Time period (real data)	from 05:30:16 to 05:36:06 UTC	from 05:27:24 to 05:34:40 UTC





340 FIG. 4. PPI scans of radar reflectivity from (a) the RCSL at the elevation angle of 1 degree and (b) the RCWF  
 341 at 0.483 degree. (c) and (d) are the Doppler velocity observed by the RCSL and the RCWF at the same elevation  
 342 angles as (a) and (b), respectively.

343 *c. Assessment of accuracy*

344 The accuracy of the retrieved results against the true variables is evaluated using the spatial  
 345 correlation coefficient (SCC), and the root-mean-square error (RMSE), including horizontal wind  
 346 field ( $u$  and  $v$  combined), vertical wind, and the first derivative of the wind field: divergence, and  
 347 vorticity, are computed (Liou et al. 2012).

$$SCC(A) = \frac{(A_r - \bar{A}_r)(A_t - \bar{A}_t)}{\sqrt{(A_r - \bar{A}_r)^2(A_t - \bar{A}_t)^2}} \quad (3)$$

$$RMSE(A) = \sqrt{\frac{\sum (A_r - A_t)^2}{M}} \quad (4)$$

348 The subscripts “r” and “t” denotes the “retrieved” and “true” quantities, and  $M$  is the total number  
 349 of grid points used in the computation.  $\bar{A}$  denotes the value of the domain average.

#### 350 4. Sensitivity tests

351 In this section, we perform a series of sensitivity experiments to assess the impact of various  
 352 factors on the accuracy of wind retrieval, including a) the prescribed strength of Neumann and  
 353 Dirichlet boundary constraints, b) the smoothness of complex terrain slope, c) the algorithm  
 354 assumptions of mass continuity and terrain boundary, and d) the grid spacing and Gaussian  
 355 recursive filter setting. The purpose of each sensitivity test will be explained in its respective  
 356 subsection. All the experiments herein are solely based on the input resampled observations and  
 357 assumed boundary conditions. The first guess background wind field is set to be zero.

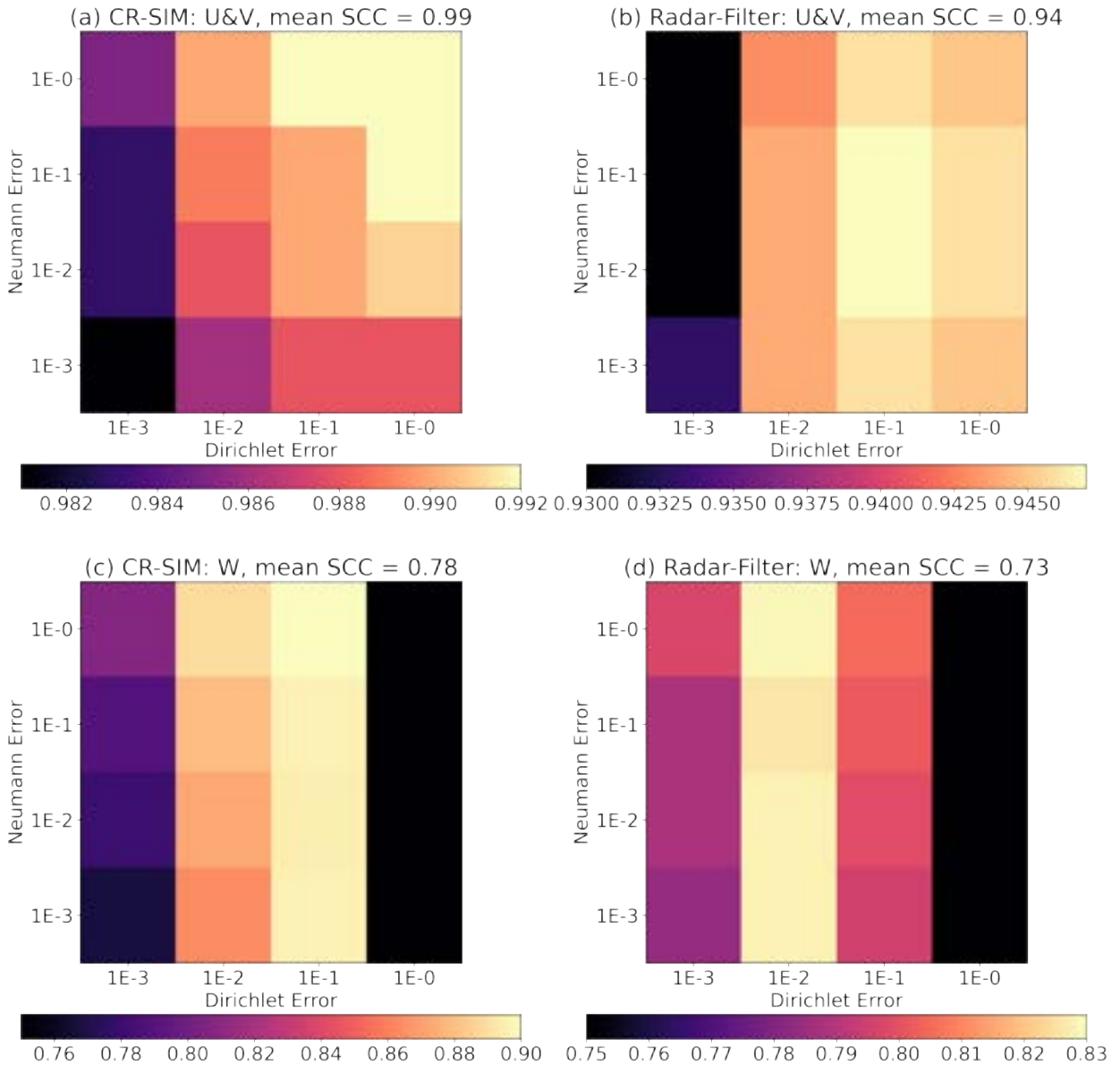
##### 358 *a. Sensitivity of the prescribed strength of Neumann and Dirichlet boundary constraints*

359 Previous wind retrievals over complex techniques enforce the wind blocked and induced by  
 360 topography to follow the terrain morphology according to the underlying physical understanding.  
 361 Since SAMURAI offers the flexibility to adjust the strictness of the terrain boundary assumptions  
 362 of surface impermeability and topographic forcing, this sensitivity experiment is conducted to  
 363 explore the effectiveness of the assumption of boundary conditions compared to other methods  
 364 that explicitly integrate any physical constraints. Table 1 displays the various experimental setups  
 365 and their associated labels discussed in this subsection. The prescribed strength of the boundary  
 366 constraint errors ranges from  $1 \times 10^{-3}$  (1E-3) to  $1 \times 10^0$  (1E-0), and is applied to every data point  
 367 at the terrain height. The prescribed strength of the constraint differs between the Neumann and  
 368 the Dirichlet boundaries but the mean slope is kept the same. This setup results in 16 experiments  
 369 for the CR-SIM and Radar-Filter datasets respectively, as shown in the second and third columns  
 370 of Table 1.

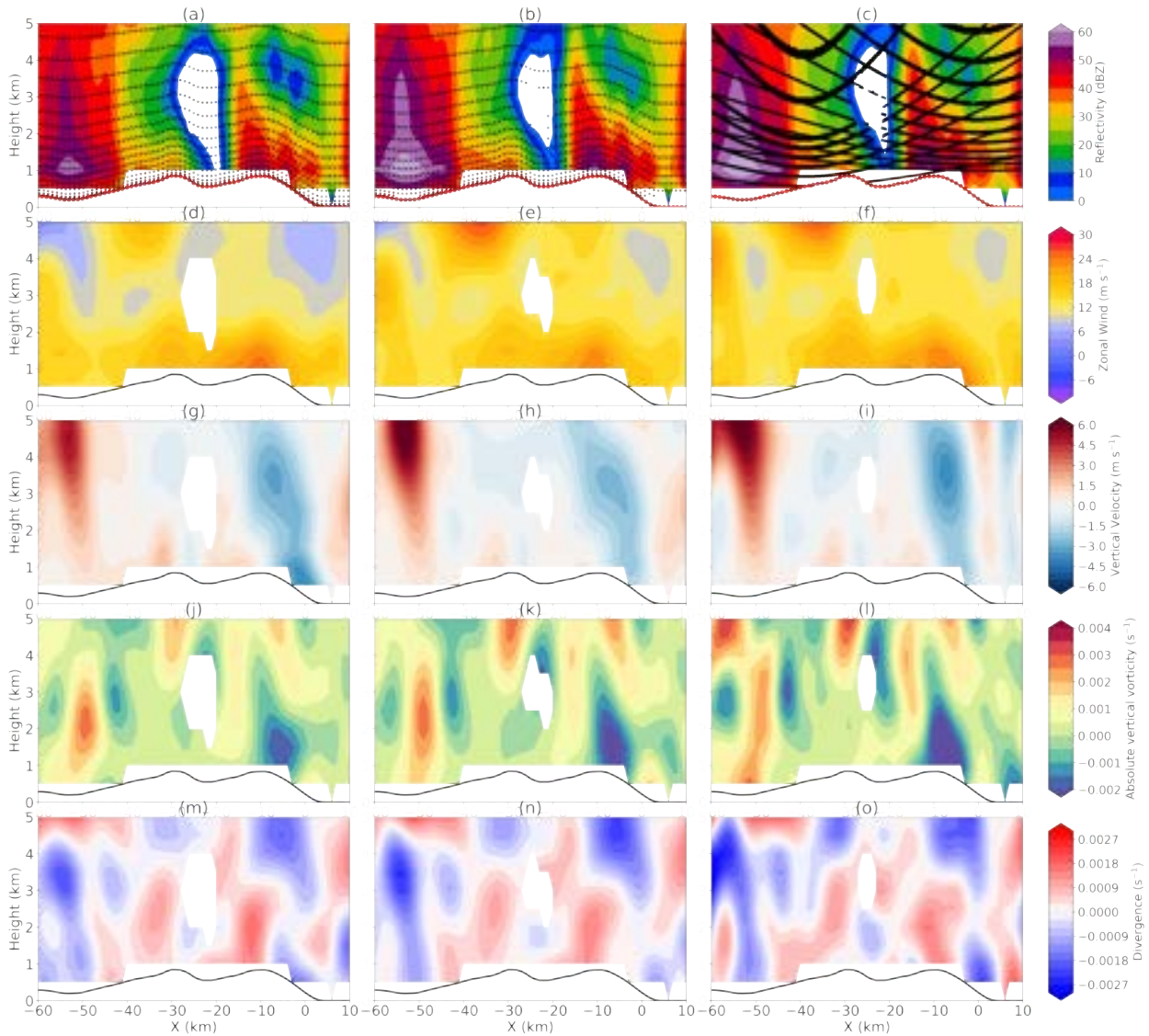
371 Figure 3 shows the SCC scores of the CR-SIM and radar-filter datasets with various strengths  
372 of boundary errors. The CR-SIM experiments with different prescribed terrain boundary errors  
373 all outperform the radar-filter experiments in terms of the three-dimensional wind, divergence,  
374 and vorticity fields. The CR-SIM experiments show that relaxing the pseudo-observational errors  
375 provided by the boundary can retrieve a horizontal wind field similar to the reference data with an  
376 accuracy of up to 0.992. The average SCC score for the horizontal wind across all 16 sensitivity  
377 tests is 0.99, indicating a high fidelity of the horizontal wind retrieval from the Doppler velocity  
378 when sufficient data is available within the domain of interest. On the other hand, the retrieval of  
379 vertical wind is highly sensitive to the strength of imposing boundary conditions. If the Dirichlet  
380 error is relaxed to  $1 \times 10^0$ , which is approximately two orders higher than the averaged terrain slope  
381 ( $6 \times 10^{-2}$ ), the SCC score is less than 0.78 and shows no sensitivity to the order of the Neumann  
382 boundary error. When a strong Dirichlet boundary condition with an error of  $1 \times 10^{-3}$  is imposed,  
383 the SCC score drops below 0.76. However, setting the Dirichlet error to  $1 \times 10^{-1}$ , which is only  
384 one order higher than the averaged terrain slope, allows the SCC score to reach as high as 0.9.  
385 The CR-SIM results highlight the importance of setting the Dirichlet error to a similar order as the  
386 terrain slope map for accurate wind field reconstruction, while the Neumann error has less impact  
387 on the retrievals in our experiments when the data distribution and coverage are sufficient. The  
388 performances of the horizontal divergence and vertical vorticity are similar to the horizontal wind  
389 retrieval result and are relatively insensitive to the different orders of boundary errors (not shown).  
390 This experiment suggests that the Doppler error caused by the Doppler projection has minimal  
391 effect on the horizontal wind retrieval, but it has a more significant impact on the vertical wind due  
392 to its reliance on the mass continuity equation and topographic forcing assumptions.

393 The average SCC score for the radar-filter sensitivity experiments is 0.94 for horizontal wind  
394 retrieval and 0.73 for vertical wind retrieval. These scores are approximately 0.05 lower than the  
395 CR-SIM results, primarily due to the limited number of data points resulting from the designed  
396 VCP. Interestingly, the highest SCC score for the horizontal wind field is observed in the NE-1DE-1  
397 experiment, while higher SCC scores for the vertical wind are mainly found in experiments with  
398 a  $1 \times 10^{-2}$  Dirichlet error, which is approximately the same order as the average slope of the  
399 terrain map. The shifting pattern compared to the CR-SIM experiments suggests that the strength

400 of imposed terrain boundary conditions becomes more critical when there is less data close to the  
 401 surface and sparse data distribution.



402 FIG. 5. The SCC scores of the wind field retrieved from the CR-SIM dataset are shown in (a) and (c), while  
 403 the scores from the radar-filter dataset are shown in (b) and (d). In (a) and (b), the scores represent the horizontal  
 404 wind, while in (c) and (d), the scores represent the vertical wind. The scores are computed using all the data  
 405 points from the surface to 5 km within the blue box indicated in Figure 3.



406 FIG. 6. Comparison of the “truth”, CR-SIM: NE-1DE-1, and radar-filter: NE-1DE-1 retrieval output (from left  
 407 to right) with the vertical cross sections of reflectivity, zonal wind, vertical velocity, absolute vertical vorticity,  
 408 and divergence (from top to bottom). The vertical cross section is the green line denoted in Fig. 3. The black  
 409 dot denotes the data distribution, and the red dot denotes the pseudo-observations imposed by the Neumann and  
 410 Dirichlet boundary conditions at the terrain height. The black line denotes the topography.

411 Considering the SCC and RMSE results (not shown), the NE-1DE-1 experiment demonstrates  
 412 the best retrieval performance for this particular radar configuration and data distribution. Figure  
 413 6 illustrates a comparison of the same vertical cross section among the “truth”, the CR-SIM NE-  
 414 1DE-1 experiment, and the radar-filter NE-1DE-1 experiment (green line denoted in Fig. 3). A

415 strong convective core with 60 dBZ at  $X = -55$  km is associated with a  $5 \text{ m s}^{-1}$  updraft at  $z =$   
416 5 km. While the retrieved vertical velocities from both the CR-SIM and radar-filter experiments  
417 overestimate this specific updraft, the overall pattern closely resembles the reference. The zonal  
418 wind exhibits an enhanced upslope wind with divergence over the hill, accompanied by a downdraft  
419 down the hill and negative vorticity from  $X = -30$  to 0 km. Although the CR-SIM and radar-filter  
420 experiments do not precisely capture the amplitude as expected due to Doppler errors, radar beam  
421 geometry, and limited data, they successfully resolve the physical and qualitative aspects of the  
422 feature of interest. It is important to note that in cases where data is sparse and the geometry of  
423 the dual-Doppler beams is poor ( $X = 0 - 5$  km), there is a potential for the creation of artificial  
424 weak updrafts and downdrafts. Nonetheless, the overall analysis effectively captures our scale of  
425 interest.

426 Figure 7 shows another example of a vertical cross section across the snow mountain ridge,  
427 denoted by the white line in Fig. 3. The shallow convection is associated with positive vorticity  
428 and upslope wind, with a  $2 \text{ m s}^{-1}$  updraft and shallow convergence close to the ground. A jet with  
429  $\approx 32 \text{ m s}^{-1}$  at  $z = 3$  km is over the peak of the hill. A jet with a velocity of approximately  $32 \text{ m}$   
430  $\text{s}^{-1}$  at  $z = 3$  km is located over the peak of the hill. Both the CR-SIM and radar-filter NE-1DE-1  
431 experiments capture the pattern, although they slightly underestimate the downdraft magnitude at  
432 the lee side and overestimate the amplitude of the jet aloft and its position. The radar-filter NE-  
433 1DE-1 experiment exhibits a strong updraft at a height of 5 km (between  $X = 0$  and 5 km), which  
434 is due to the absence of data close to the ground, leading to the dominance of the mass continuity  
435 equation in the retrieval of vertical velocity in that region. Nevertheless, the retrievals with terrain  
436 boundary implementations can capture the scale of interest and provide a good representation of  
437 mesoscale features.

440 In order to address the sensitivity of different prescribed strengths of the boundary constraints,  
441 Figure 8 presents the impact of these constraints on the vertical velocity and vorticity patterns along  
442 the same vertical cross sections as shown in Figs. 6 and 7. When the Dirichlet boundary condition  
443 is relaxed, enhanced vertical motion is predominantly observed above 3 km in both cross sections.  
444 This behavior is dictated by the mass continuity assumption, which governs the retrieval pattern  
445 of vertical motion. On the other hand, the imposition of a strict Dirichlet boundary constraint  
446 enhances the influence of the terrain boundary on the vertical wind retrieval. This is evident in

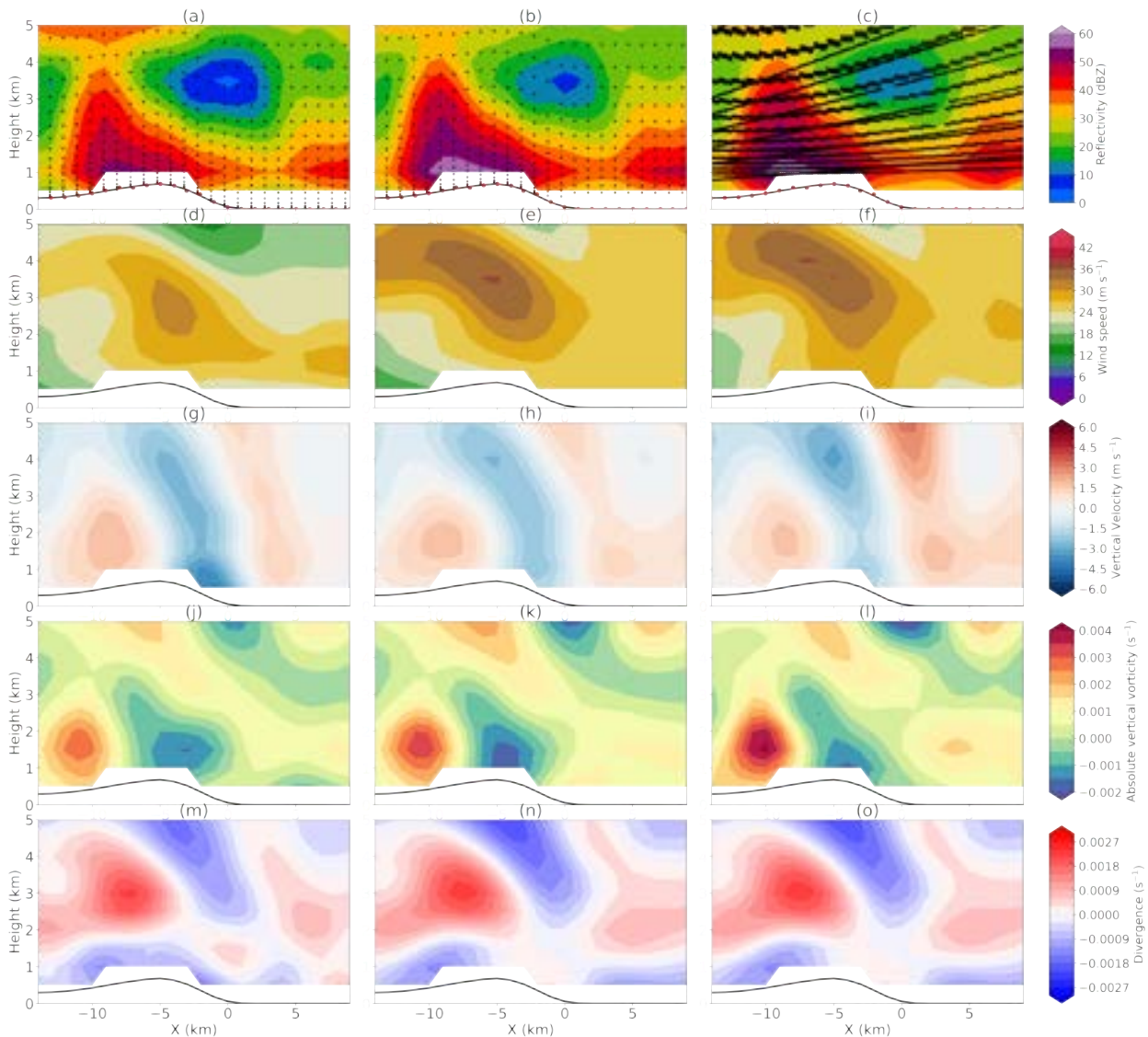
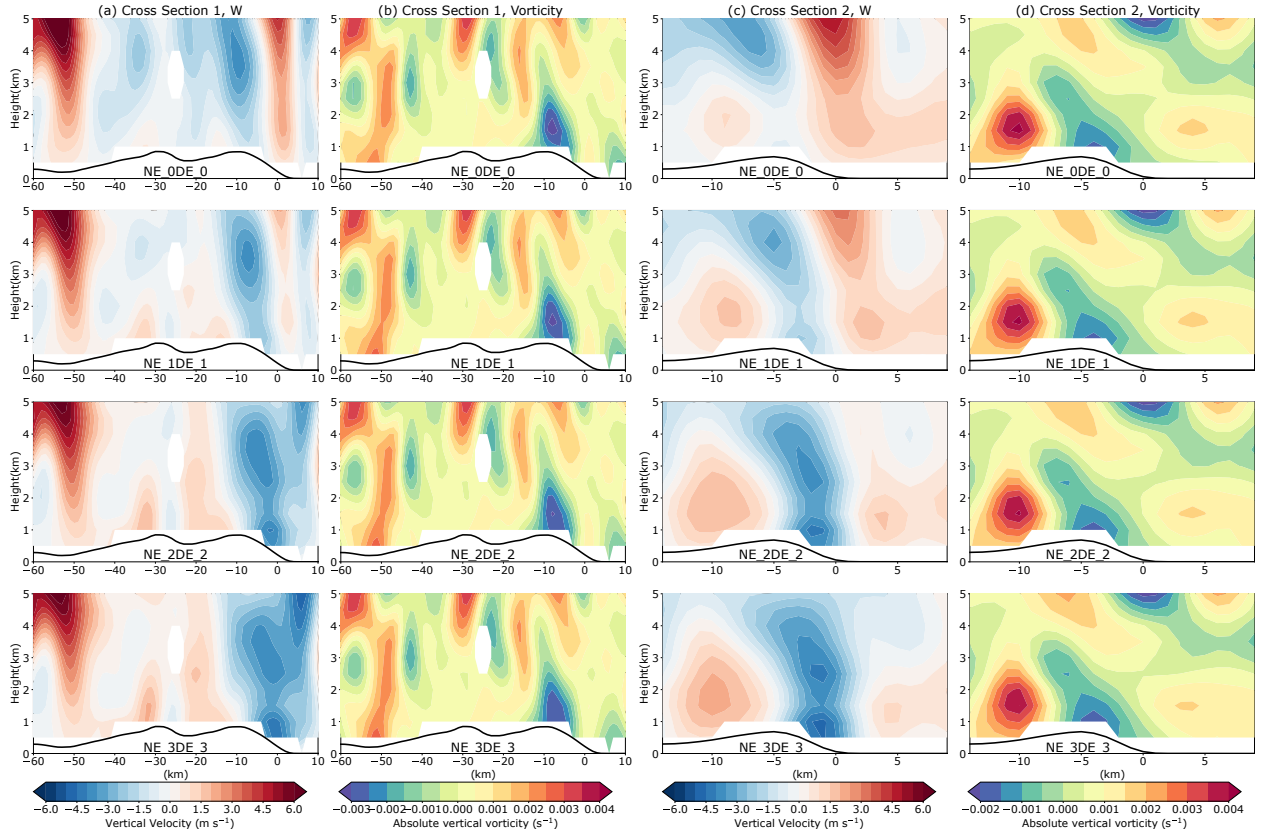


FIG. 7. Similar to Fig. 6 but for the vertical cross section along the white line denoted in Fig. 3.

447 the retrieval's ability to capture the enhanced downward motion locked to the terrain between -3  
 448 and 2 km, as seen in Figs. 7g and 8c, compared to the reference truth. The figure highlights that  
 449 variations in the imposed Dirichlet boundary constraint result in notable changes in the vertical  
 450 motion retrieval.

451 Regarding the absolute vertical vorticity, the retrievals from all experiments exhibit good agree-  
 452 ment with the reference when there is sufficient data point coverage. The retrievals correctly  
 453 identify regions of elongated positive vorticity from the surface to 3 km, positioned between two  
 454 regions of negative vorticity, as seen in cross section 1 (Fig. 8b). Additionally, an enhanced



438 FIG. 8. Comparison of the NE-0DE-0, NE-1DE-1, NE-2DE-2, NE-3DE-3 experiments (from the top row to  
 439 the bottom). Vertical cross sections of (a), (c) vertical velocity and (b), (d) absolute vertical vorticity.

455 negative vorticity region is identified on top of the peak between  $X = -10$  and  $0$  km in cross section  
 456 1. Cross section 2 (Fig. 8) shows that the vorticity couplet close to the surface between  $X = -15$  and  
 457  $0$  km is correctly identified, albeit with a slightly stronger amplitude compared to the reference.  
 458 Although the amplitude is slightly off, the general vorticity pattern is well-captured.

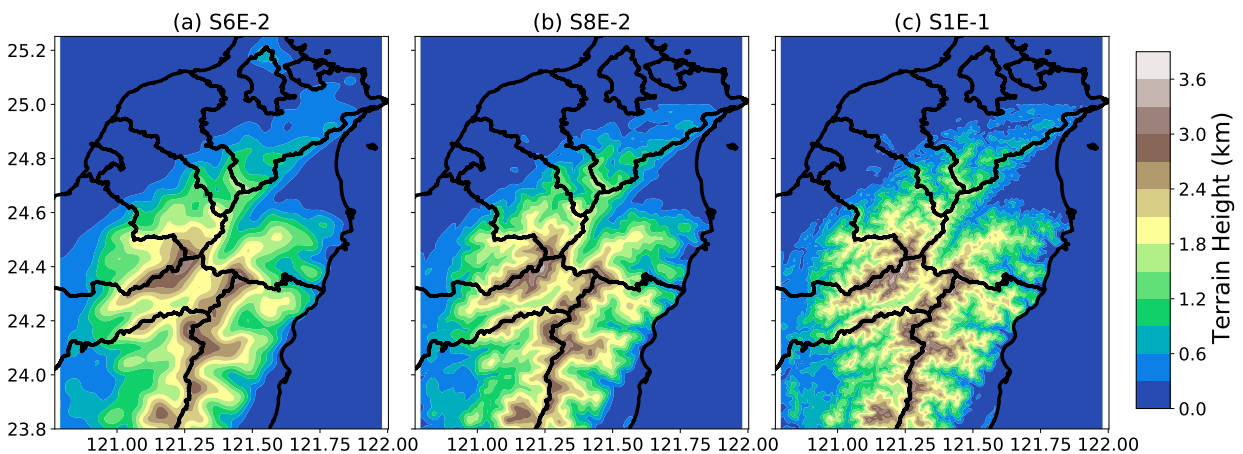
459 The sensitivity experiment results indicate the importance of prescribed boundary constraints  
 460 in achieving an improved vertical wind structure. The error order of the prescribed boundary  
 461 constraint depends on the density and distribution of data points near the surface. When data  
 462 points are sufficient and close to the surface, the prescribed Neumann boundary constraint may  
 463 have limited impact on the overall retrieval, while the Dirichlet boundary condition becomes more  
 464 influential in the vertical wind retrieval. Although our results demonstrate that the best retrieval  
 465 occurs when the prescribed boundary constraint has a similar order to the averaged terrain slope,



466 it is important to note that this finding is specific to the examined radar geometry, and the exact  
467 numerical errors may vary in other scenarios.

468 *b. Sensitivity of the smoothness of complex terrain slope*

469 Orographic rainfall is sensitive to several factors, including mountain dimensions, cross-barrier  
470 flow, moist static stability, and microphysical processes. An idealized two-dimensional modeling  
471 study conducted by Colle (2004) found that the orographic precipitation is dependent on the  
472 dimensions of the mountain when the cross-barrier flow is less than  $20 \text{ m s}^{-1}$ . Kirshbaum and  
473 Durran (2005), using quasi-idealized numerical simulations, demonstrated that low-amplitude  
474 smooth topographic roughness can effectively act as prominent sub-scale peaks, triggering and  
475 organizing banded orographic precipitation. They also found that the bands created by isolated  
476 peaks can be sensitive to the location of those irregular peaks relative to the main ridge. In  
477 contrast, a recent study by Singh et al. (2021) suggests that using high-resolution topography in the  
478 model has the potential to reduce biases in the local-scale dynamics related to orographic features.  
479 Although our WRF simulation uses a terrain resolution of 30-arc seconds (approximately 1 km)  
480 with an average mean slope of  $6 \times 10^{-2}$  (S6E-2 experiment, Table 1), which represents the physical  
481 scale resolved by the model, it is still worthwhile to investigate the sensitivity of the retrieval when  
482 using terrain maps with different degrees of smoothing and filtering.



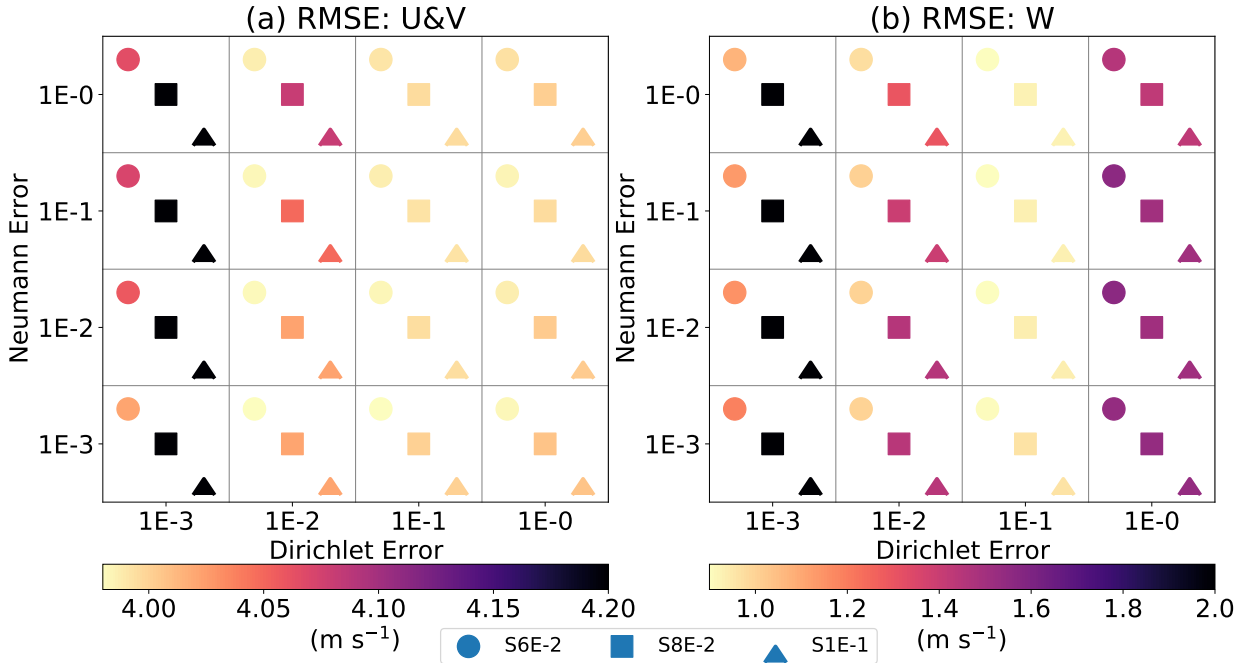
483 FIG. 9. Complex terrain in Taiwan with different average slopes: (a) S6E-2 ( $6 \times 10^{-2}$ ), (b) S8E-2 ( $8 \times 10^{-2}$ ),  
484 and (c) S1E-1 ( $1 \times 10^{-1}$ ).

485 The Advanced Spaceborne Thermal Emission and Reflection Radiometer Global Digital Ele-  
486 vation Map (ASTER GDEM) was generated using stereo-pair images collected by the ASTER  
487 instrument (Spacesystems and Team 2019). The ASTER GDEM data has a horizontal resolution  
488 of 1 arc-second ( $\approx 30$  m) grid of elevation data. To match the scale of interest and reduce computa-  
489 tional time, we employ two methods to align the 1 arc-second data with the 30 arc-second grid. The  
490 first method involves applying Fast Fourier Transform (FFT) to the ASTER GDEM data, removing  
491 wavenumbers lower than 33, and preserving approximately 1 km features. This terrain map exhibits  
492 an averaged terrain slope of  $8 \times 10^{-2}$  (S8E-2 experiment), closely resembling the terrain map in the  
493 WRF simulation while retaining some irregular peaks. The second method involves sub-sampling  
494 the ASTER GDEM data and performing nearest neighbor interpolation from high-resolution to  
495 low-resolution. This approach preserves most of the peaks with steeper slopes compared to other  
496 methods, resulting in a terrain map with an averaged terrain slope of  $1 \times 10^{-1}$  (S1E-1 experiment).

497 Figure 9 depicts the complex terrain with varying terrain slopes, and the details of the experimen-  
498 tal setup can be found in Table 1. Among the three, the S6E-2 experiment exhibits the smoothest  
499 terrain, while the S1E-1 preserves the most intricate features. The sensitivity test in this section  
500 also varies the strength of Neumann and Dirichlet boundary constraints to explore the relationship  
501 between the boundary conditions and terrain slope features. The sensitivity test in this section  
502 also investigates the impact of varying the strength of Neumann and Dirichlet boundary constraints  
503 under different terrain slope features on the retrieval results.

504 Figure 10 shows the RMSE results from the sensitivity experiments. Using the terrain slope  
505 corresponding to the simulation yields the lowest RMSE for the wind field as expected, since  
506 the original terrain map provides a better representation of the phenomenon at the desired scale.  
507 Among the three experiments, the S1E-1 retrieved wind exhibits the highest RMSE. In the S1E-1  
508 experiment, the horizontal and vertical retrievals show the best performance when the Dirichlet  
509 constraint is prescribed with a  $1 \times 10^{-1}$  error. The S8E-2 experiment demonstrates a similar  
510 pattern to the S1E-1 experiment but with a lower RMSE. Notably, all the experiments conducted  
511 here exhibit a lower sensitivity to the Neumann boundary error, likely due to an appropriate Doppler  
512 radar geometry setup in the region of interest.

516 Figure 11 displays the vertical cross sections obtained from the S6E-2, S8E-2, and S1E-1  
517 experiments, with a Neumann and Dirichlet boundary error of  $1 \times 10^{-1}$ . The overall patterns are

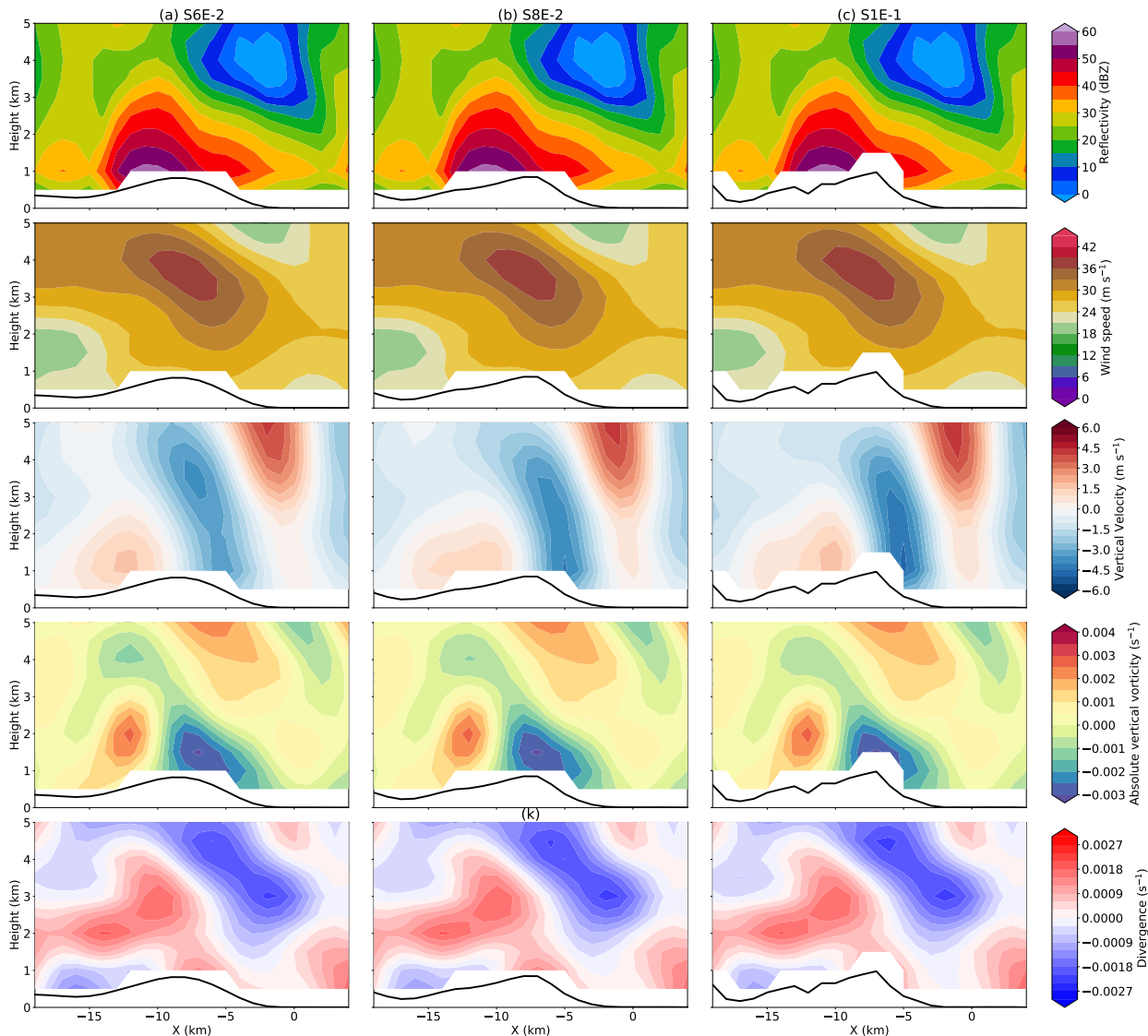


513 FIG. 10. Scatter plot showing the RMSE of the (a) horizontal wind and (b) vertical wind from the S6E-2,  
 514 S8E-2, and S1E-1 experiments with different specified terrain boundary condition errors. The color shading of  
 515 the dots represents the magnitude of the RMSE.

518 similar among the three experiments and consistent with the model in general, aligning with the  
 519 findings of Kirshbaum and Durran (2005). In the experiments with steeper and more detailed  
 520 terrain, an enhanced downdraft near the terrain peak (between  $X = -8$  and  $-3$  km) is observed in  
 521 the S8E-2 and S1E-1 experiments, with the S1E-1 experiment exhibiting a magnitude of up to  $5.5$   
 522  $\text{m s}^{-1}$ . The divergence field indicates an intensified convergence at a height of  $4.5$  km between  $X$   
 523  $= -8$  and  $-3$  km in the S8E-2 and S1E-1 experiments, suggesting that the influence of the steepness  
 524 of the terrain slope can extend to higher altitudes, rather than being confined to the lower levels.  
 525 These sensitivity experiment results emphasize the importance of using a terrain map that aligns  
 526 with the desired scale of interest for accurate wind field reconstruction.

530 *c. Sensitivity of the algorithm assumptions of mass continuity and terrain boundary*

531 The traditional method for retrieving vertical air motion involves solving the integral mass  
 532 continuity equation by integrating upwards from the bottom level and/or downwards from the  
 533 top level (Ray et al. 1980; Protat and Zawadzki 1999). This approach requires an estimation of



527 FIG. 11. Same vertical cross section as shown in Figure 7, but for the (a) S6E-2, (b) S8E-2, and (c) S1E-1  
 528 experiments with a  $1 \times 10^{-1}$  error for the Neumann and Dirichelt boundary conditions. The black line represents  
 529 the terrain height along the cross section.

534 horizontal wind divergence at each level, and errors in horizontal wind divergence can propagate  
 535 and accumulate throughout the column, leading to larger errors in the retrieved vertical velocity.  
 536 The variational approach has been shown to be less sensitive to the specification of boundary  
 537 conditions for vertical velocity retrieval (Gao et al. 1999; Potvin et al. 2012a), but the sensitivity  
 538 of vertical wind retrieval regarding the mass continuity and the terrain boundary constraints have  
 539 not been explored before. In this experiment, we explore the algorithm assumptions of the mass

540 continuity equation and terrain boundary conditions through three types of experiments: WM-NT  
 541 (With the Mass continuity, No Terrain boundary condition), NW-WT, and WM-WT (With Mass  
 542 continuity, With Terrain boundary condition). The experimental configuration is detailed in Table  
 543 3.

544 TABLE 3. Configuration of different experimental setups for testing the sensitivity of mass continuity and the  
 545 terrain boundary conditions for three-dimensional wind retrieval. The prefix WM (with the mass continuity) or  
 546 NM (no mass continuity) indicates whether mass continuity is activated or not. Similarly, the prefix WT (with  
 547 the terrain boundary condition) or NT (no terrain boundary condition) indicates whether the terrain boundary  
 548 condition is activated or not.

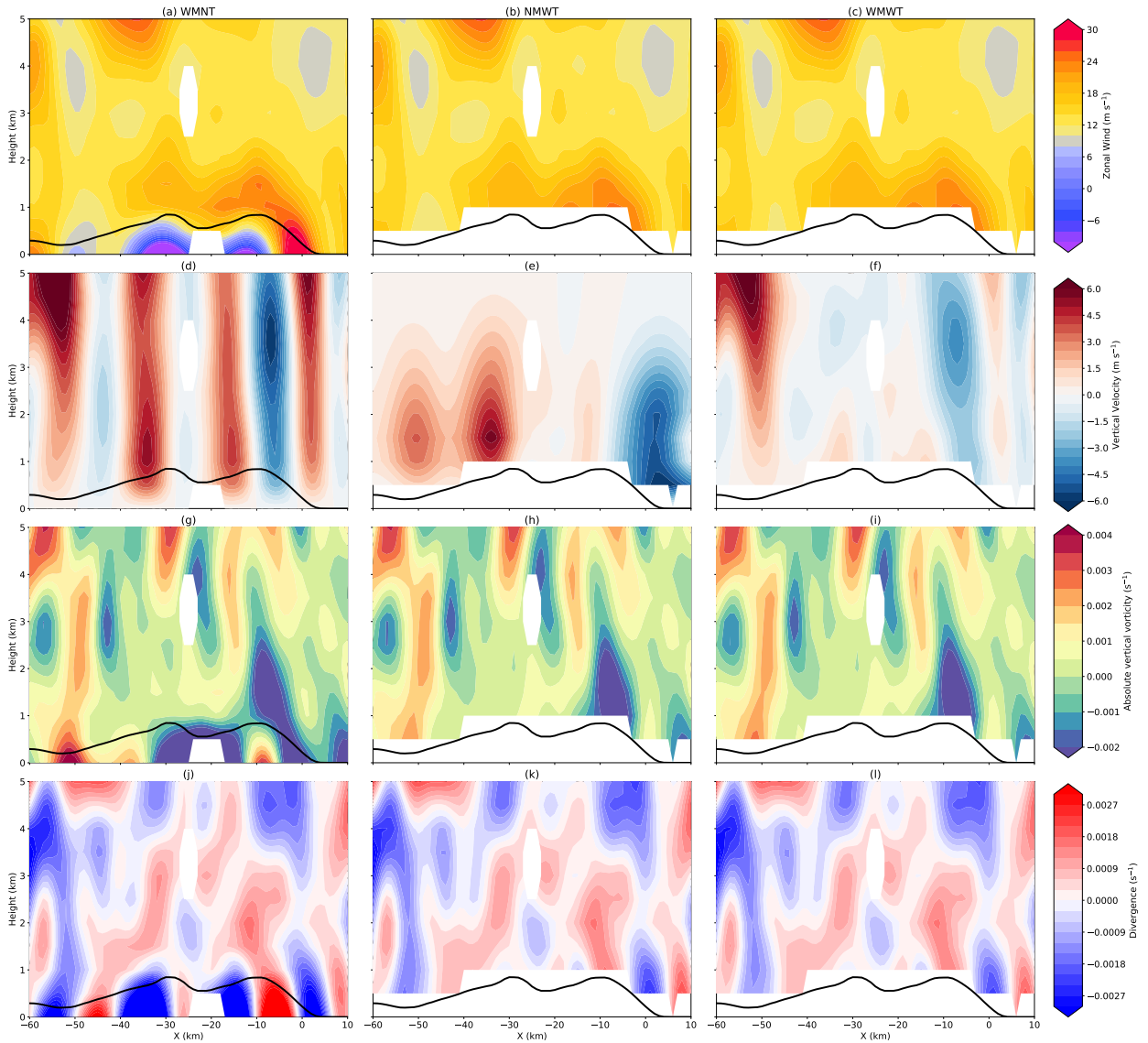
Name	Mass Continuity, Error	Terrain boundary, (Neumann Error, Dirichlet Error)
WM-NT	Yes, 1	No, (N/A,N/A), $w = 0 \text{ m s}^{-1}$ at $z = 0 \text{ km}$
NM-WT	No, N/A	Yes, (1E-1, 1E-1)
WM-WT	Yes, 1	Yes, (1E-1, 1E-1)

549 Figure 12 shows the vertical cross section 1 obtained from the experiments. First of all, the  
 550 WM-NT experiment exhibits artificial wind below the terrain, characterized by weak zonal wind  
 551 and vertical velocity near the ground. The occurrence of artificial wind below the terrain is a result  
 552 of interpolating the missing data area to  $z = 0 \text{ km}$  using cubic-B splines and the Gaussian recursive  
 553 filter in order to satisfy the boundary condition that the vertical wind is  $0 \text{ m s}^{-1}$ . Second, the  
 554 WM-NT result shows a similar pattern as the other two in the horizontal wind field, vorticity, and  
 555 divergence when the retrieval is above the terrain. The zonal wind near the terrain height, between  
 556  $X = -5$  and  $5 \text{ km}$ , reaches speeds up to  $30 \text{ m s}^{-1}$ , whereas the WM-WT retrieval shows zonal  
 557 wind of only  $25 \text{ m s}^{-1}$ . Third, the lack of terrain boundary constraints has a significant impact  
 558 on the retrieval of vertical wind. The WM-NT experiment produces four strong updrafts with an  
 559 approximate magnitude of  $6 \text{ m/s}$  and one downdraft with a magnitude of  $5 \text{ m s}^{-1}$  peaking at a  
 560 height of  $3.5 \text{ km}$ . While the WM-NT experiment captures the two uphill updrafts (one between  
 561  $X = -40$  and  $-30 \text{ km}$ , and the other between  $X = -20$  and  $-10 \text{ km}$ ), their amplitudes are excessively  
 562 strong, and the vertical motion extends too far upward compared to the reference. In the NM-  
 563 WT experiment, the horizontal wind, vorticity, and divergence fields are in good agreement with  
 564 the WM-WT experiment, similar to the WM-NT case. The enhanced vertical velocity is closely  
 565 coupled with the terrain, and the vertical velocity remains close to zero above a height of  $4 \text{ km}$ .

566 Figure 13 presents the results of vertical cross section 2. The overall findings are consistent  
567 with those in Fig. 12, but one notable feature is the presence of a weak updraft (between -10 and  
568 -5 km) associated with upslope wind, which is not captured by the WM-NT experiment. These  
569 unresolved wind features along the slope arise from the assumption of  $w = 0 \text{ m s}^{-1}$  at  $z = 0 \text{ km}$ .  
570 This assumption leads to strong divergence and the formation of a low-level jet below the terrain,  
571 so a compensating downdraft aloft counteracts the upward motion. In the NM-WT experiment, a  
572 much stronger downdraft of up to  $-6 \text{ m s}^{-1}$  is observed, which is shifted downhill and closer to  
573 the surface compared to the WM-WT experiment. These experiments highlight the necessity of  
574 considering the assumptions of the mass continuity and the terrain boundary condition to obtain  
575 an accurate and realistic representation of the vertical wind field.

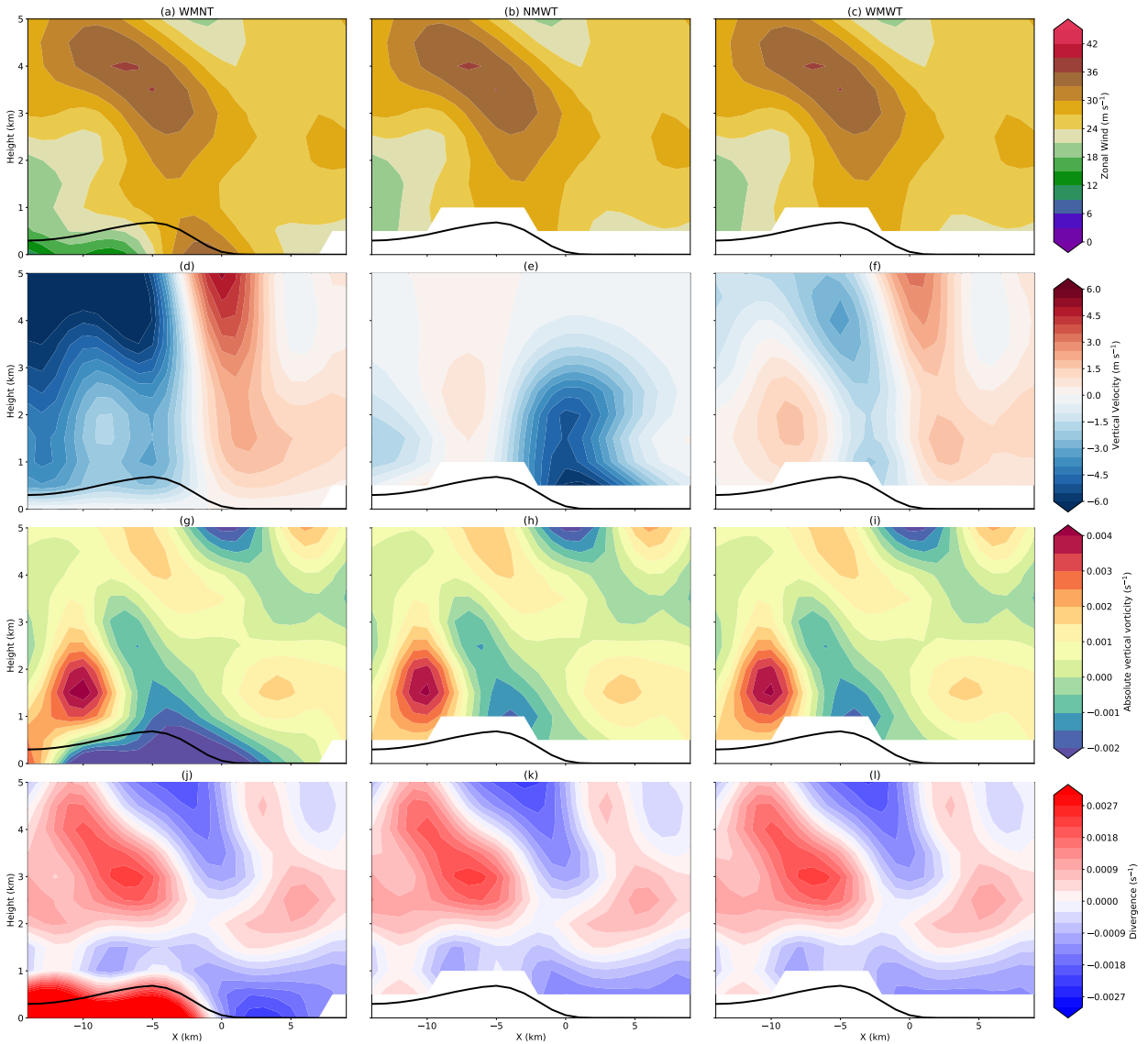
#### 582 *d. Sensitivity to the grid spacing and Gaussian recursive filter setting*

583 In principle, a minimum of five grid points is required to represent a wave on a grid to ensure that  
584 the resolvable wave is on a scale of 2 times the data spacing  $\Delta n$  (Koch et al. 1983). To accurately  
585 represent a resolvable wavelength,  $\Delta x$  should then not exceed half of  $\Delta n$ . Regarding the lower limit,  
586 it is not recommended to have an overly fine grid spacing, as calculations of derivative quantities  
587 become sensitive to the grid length and the computations become more expensive. Therefore,  
588 the empirical ratio between the grid spacing ( $\Delta x$ ) and the data spacing ( $\Delta n$ ), denoted as  $\Delta x/\Delta n$ ,  
589 falls within the range of 1/3 to 1/2, as suggested by the Barnes objective technique Koch et al.  
590 (1983). In SAMURAI, the resolved wind field is a function composed of finite elements. The  
591 grid-spacing determines the minimum spatial scale resolved by the cubic B-spline function. The  
592 Gaussian filter produces a Gaussian response to a point observation but can dampen the amplitude  
593 of lower wavelengths and make the retrieval less sensitive to noise. The Gaussian filter setting  
594 determines the length scale in grid points, and a higher value can result in larger spatial influence of  
595 the observations and additional smoothing. Choosing an appropriate combination of grid spacing  
596 and filter settings is crucial to retrieve the best representation of the desired scale of interest. For  
597 example, since our scale of interest is approximately 4 km, the grid spacing can be set to 1 km, and  
598 the Gaussian filter is set to 4. Alternatively, the grid spacing can be set to 2 km, and the Gaussian  
599 filter is set to 2. Both settings can provide a good representation of the scale of interest with slightly  
600 different results, and features and noise with wavelengths less than 4 km will be damped.



576 FIG. 12. Same vertical cross section as shown in Figure 6, but for the (a) WM-NT, (b) NM-WT, and (c)  
 577 WM-WT experiments, displaying zonal wind, vertical velocity, absolute vertical vorticity, and divergence from  
 578 top to bottom. The black line represents the terrain height along the cross section.

601 Observations inherently include a certain level of noise, and applying a Gaussian filter can help  
 602 smooth out this noise. For a well-resolved Doppler geometry, the uncertainty in the wind field  
 603 should be less than  $2 \text{ m s}^{-1}$  (Hildebrand et al. 1996). To explore the sensitivity of the grid spacing  
 604 and Gaussian recursive filter setting, we add Gaussian noise with 1 standard deviation of the  
 605 Doppler velocity for the WRF input data, considering the sub-grid scale turbulence and Doppler



579 FIG. 13. Same vertical cross section as shown in Figure 7, but for the (a) WN-NT, (b) NM-WT, and (c)  
 580 WM-WT experiments, displaying wind speed, vertical velocity, absolute vertical vorticity, and divergence from  
 581 top to bottom.

606 velocity instrument noise. A sensitivity test of different grid spacing and the length of filter setup  
 607 is shown in Table 4.

608 Figure 14 displays the results from each sensitivity experiment compared to the WRF simulation  
 609 direct output. The Grid05Filter222 configuration is designed to resolve features at a scale of  
 610 approximately 1 km. The Grid05Filter222 analysis retains more detail, but the overall retrieval is



611 noisy (Figure 14b), particularly for the vorticity and divergence fields because the derivative of the  
612 wind field is more sensitive to the wind gradient. The Gaussian filter is set to 2 nodes, which is  
613 not sufficiently strong to suppress the noise. The root mean square error (RMSE) of the vertical  
614 velocity is 0.77.

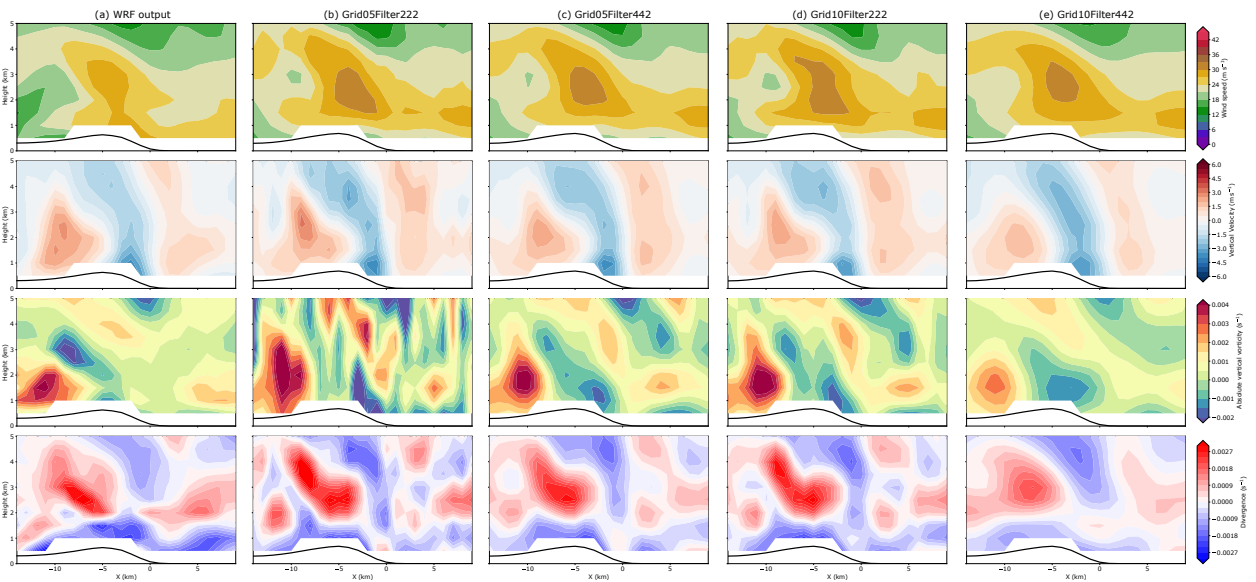
615 The Grid05Filter442 and Grid10Filter222 configurations achieve a similar horizontal resolved  
616 scale of 2 km. The Grid10Filter222 configuration retains more details, while the Grid05Filter442  
617 analysis appears smoother due to the stronger Gaussian filter that effectively suppresses more noise  
618 (Fig. 14c and d). Both the Grid05Filter442 and Grid10Filter222 configurations can capture a  
619 similar pattern to the WRF output with detailed structures and reduced noise compared to the  
620 Grid05Filter222 results. However, there are still some artificial enhanced wiggles of features due  
621 to the mismatch in the resolved scale.

622 Overall, the Grid10Filter442 configuration achieves a horizontal scale resolution of 4 km which  
623 provides the best representation of the scale of interest (Fig. 14e). Among all the tests, the  
624 Grid10Filter442 configuration exhibits the minimum root mean square error (RMSE) for both the  
625 horizontal and vertical wind, with values of 1.85 and 0.76 m s<sup>-1</sup>, respectively.

626 Since the quality and sampling of Doppler velocity strongly influence the spatial resolution,  
627 resolved scales, and accuracy of the wind and terrain boundary constraint, it is not possible to  
628 provide a specific recommendation for filter length, grid spacing, strength of the terrain boundary  
629 constraint, and the order of the terrain slope that applies universally to all cases. Based on the given  
630 sampling and theoretical understanding, setting the grid spacing to 0.5 km is more appropriate to  
631 resolve the detailed structure (Koch et al. 1983; Ooyama 1987, 2002). However, in order to align  
632 with the resolving scale of the Weather Research and Forecasting (WRF) model, a similar horizontal  
633 resolved scale of 4 km is considered more appropriate. Results from the OSSE experiments indicate  
634 that a 0.5 km horizontal grid spacing and a Gaussian recursive filter length of 4 times the grid  
635 spacing in the horizontal direction yield the most detailed structures. On the other hand, a 1 km  
636 horizontal grid spacing and the same filter length provide higher confidence in capturing both the  
637 structure and magnitude of dominant mesoscale features. The sensitivity experiments demonstrate  
638 that different analysis settings entail an inherent trade-off between level of detail and point-wise  
639 accuracy. Therefore, the choice of settings must be carefully evaluated on a case-by-case basis and  
640 their interpretations should be made accordingly when drawing scientific conclusions.

641 TABLE 4. Configuration of different experimental setups for the grid spacing and Gaussian filter setting.  
 642 “Grid05” refers to a grid spacing of 0.5 km, and “Filter222” indicates that the Gaussian filter is applied with a  
 643 setting of 2 in the i, j, and k directions, respectively. For reference, the WRF simulation has a horizontal grid  
 644 spacing of 1 km.

Name	Grid spacing (km)	Gaussian Filter setting (i, j, k)	Approximately resolved scale (km)
Grid05Filter222	0.5	(2,2,2)	1
Grid05Filter442	0.5	(4,4,2)	2
Grid10Filter222	1.0	(2,2,2)	2
Grid10Filter442	1.0	(4,4,2)	4



645 FIG. 14. Same vertical cross section as shown in Figure 7, but for the following cases: (a) WRF simulation,  
 646 (b) Grid05Filter222, (c) Grid05Filter442, (d) Grid10Filter222, and (e) Grid10Filter442.

## 647 5. Application of real data

648 This section demonstrates the applicability of the improved SAMURAI approach using real data  
 649 from Typhoon Chanthu (2021) observed by the RCSL and RCWF radars. The radar configurations  
 650 and settings are shown in Table 2. The use of real data introduces additional challenges due  
 651 to incomplete data coverage and beam blockage, especially near the ground and on the lee side  
 652 of hills in mountainous regions. Furthermore, the quality of the wind field is dependent on the  
 653 Doppler velocity quality and scanning geometry of the radars. Considering the sensitivity tests  
 654 performed on the OSSE experiments and the limitations of real radar observations, the analysis

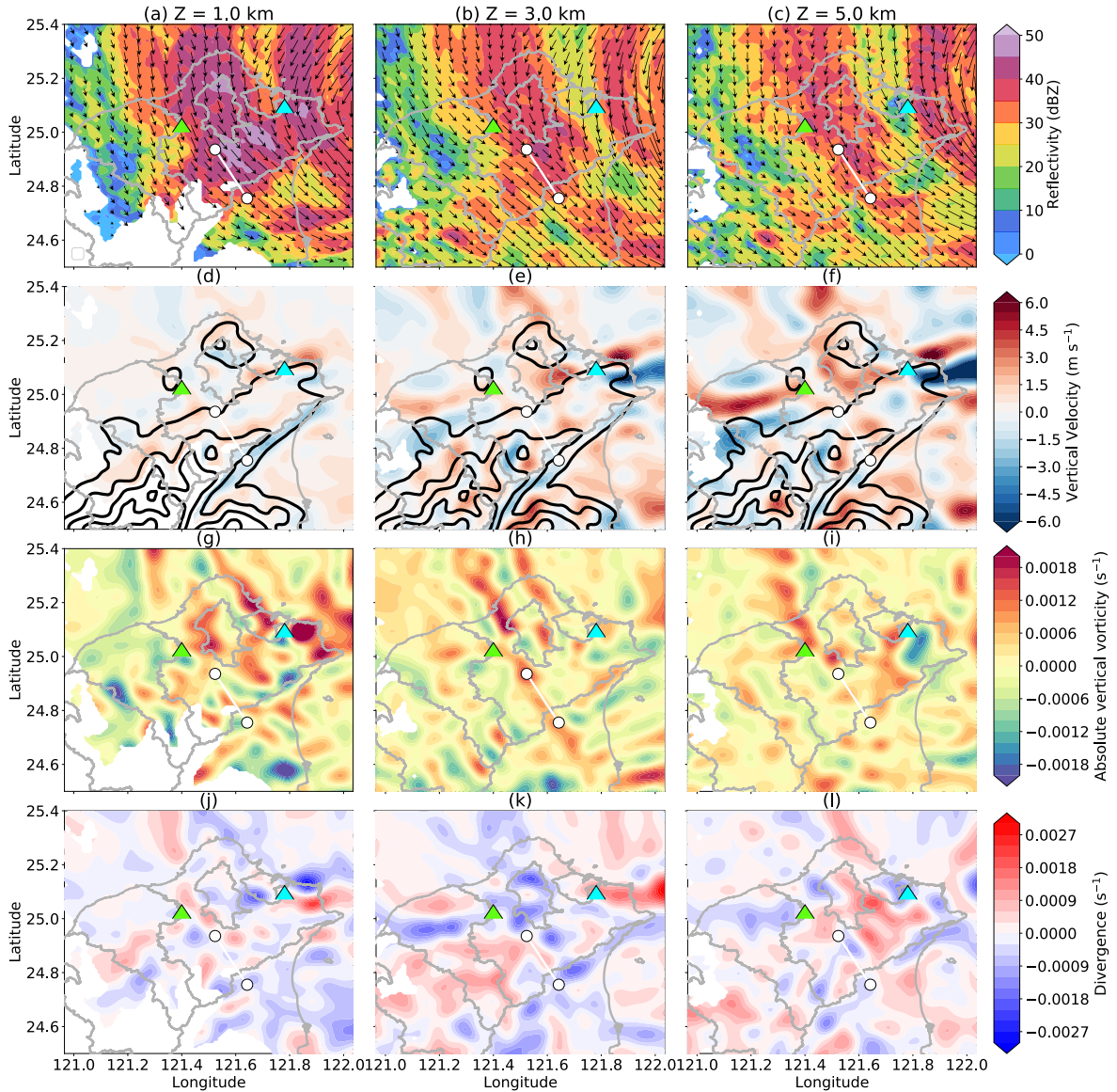
655 was performed using pseudo-observations with Neumann and Dirichlet boundary conditions with  
656 a prescribed pseudo-observational error of  $1 \times 10^{-1}$ , a terrain map with a mean slope of  $6 \times 10^{-2}$ ,  
657 a horizontal grid spacing of 1 km, a vertical grid spacing of 0.5 km, and a Gaussian recursive filter  
658 length of  $4\Delta$  nodal spacing in the horizontal dimension and  $2\Delta$  spacing in the vertical dimension.

659 The radar sweep files were processed using the Lidar Radar Open Software Environment  
660 (LROSE) software (Bell et al. 2021) and the National Center for Atmospheric Research (NCAR)  
661 SoloII software. These processing steps involved correcting Doppler velocity aliasing, as well as  
662 removing non-meteorological echoes and noise. After the editing process, the sweep files were  
663 converted to the CfRadial format in the native radar polar grid, which were used as input for further  
664 analysis.

668 Figure 15 shows the horizontal cross sections of the SAMURAI analysis. A rainband moving  
669 inland with reflectivity values over 50 dBZ suggests intense precipitation on the uphill side of the  
670 terrain. Interestingly, an elongated, thin band of downward motion parallel to the mountain range  
671 (between  $121.6$  and  $121.8$  °E,  $24.7$  and  $24.9$  °N) is found at  $z = 1$  km, collocated with a band of  
672 positive vorticity. Upward motion is most dominant on the windward side of the mountain range  
673 and increases with height, while the confidence in the wind retrievals along the baseline is lower.  
674 Considering the dual-Doppler lobes and the scarcity of data, our focus is on a specific vertical cross  
675 section indicated by the white line, which corresponds to an area with sufficient coverage of the  
676 dual-Doppler radar beams. This cross section is parallel to the rainband's horizontal wind flow,  
677 and is perpendicular to the mountain ridge, which makes it easier to assess if the retrieved wind  
678 field is physically realistic.

679 Figure 16 illustrates the vertical cross section of reflectivity, wind flow, vorticity, and divergence.  
680 In Figure 16a, a shallow reflectivity echo with a value of 50 dBZ is observed at 1 km height on  
681 the windward side. This enhanced echo extends up to 6 km height (between  $X = -20$  and  $-16$  km).  
682 Within this region, the shallow stratiform precipitation near the ground is associated with upslope  
683 wind and divergence. At 4 km height, there is convergence as shown in Figure 16e, accompanied  
684 by upward motion aloft and downward motion below, as depicted in Figure 16c. These findings  
685 align with the expected stratiform heating profile.

686 Between  $X = -16$  and  $-12$  km, as the wind flow ascends the terrain, it induces upward motion  
687 with a magnitude of  $2 \text{ m s}^{-1}$ . This upward motion is accompanied by negative vorticity ( $-0.0012$



665 FIG. 15. Horizontal cross sections of (a-c) reflectivity, (d-f) vertical motion, (g-i) absolute vertical vorticity,  
 666 (j-l) divergence. (a), (d), (g), (j) are at 1 km altitude. (b), (e), (h), (k) are at 3 km altitude, and the black contour  
 667 denotes the topography. (c), (f), (i), (l) are at 5 km altitude.

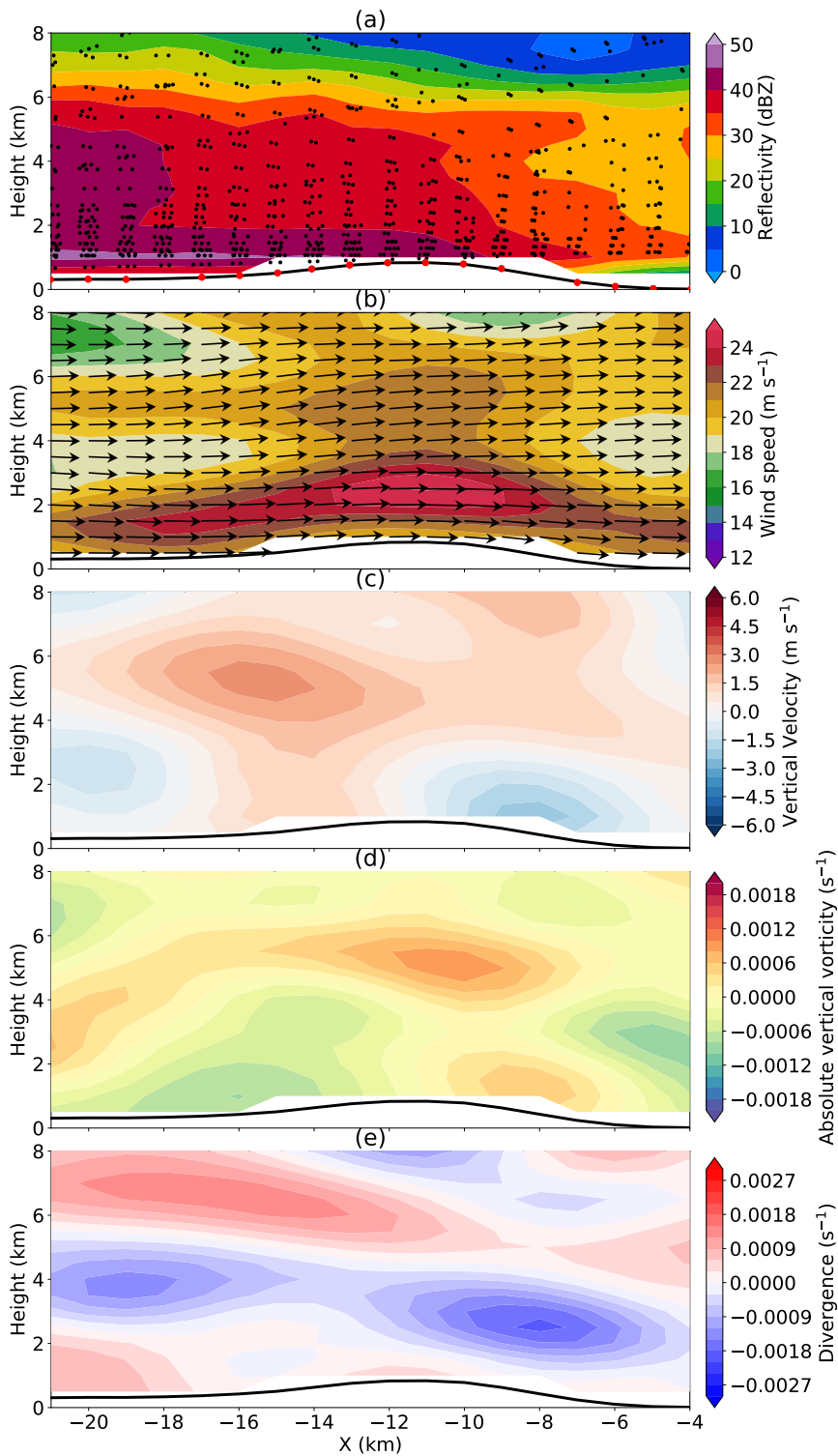
668  $s^{-1}$ ) and weak divergence near the terrain. The upward motion continues vertically and reaches  
 669 its maximum amplitude of  $5 \text{ m s}^{-1}$  at a height of 5 km. At this height, the vertical velocity  
 670 is associated with positive vorticity, convergence below, and divergence aloft. The cross-barrier  
 671 wind flow reaches its maximum at the mountain peak, exceeding  $25 \text{ m s}^{-1}$ , and decreases in the  
 672 lee. Estimates of the mountain Froude number (Smith and Barstad 2004) are greater than one,

693 indicating that the airflow successfully ascends over the mountains without significant blockage  
694 (see Cha (2023) for detailed calculation.) The results of our radar analysis are consistent with the  
695 general theoretical understanding of orographic precipitation. The flow in the lee is characterized  
696 by downward motion, positive vorticity in close proximity to the topography, and slight convergence  
697 above the ground. A comprehensive analysis of the evolution of Typhoon Chanthu's rainband and  
698 its interaction with topography is beyond the scope of the current study and will be addressed in a  
699 future study.

## 705 **6. Summary and discussion**

706 In this study, the immersed boundary method has been successfully implemented into a three-  
707 dimensional variational-based multi-Doppler radar wind synthesis algorithm. The performance of  
708 the Doppler technique is investigated using model-simulated datasets that are resampled by a radar  
709 emulator, providing a more realistic setting for the simulated radar observables. The study explores  
710 the sensitivity of various factors to assess the impact on the accuracy of wind retrieval, including  
711 a) the prescribed strength of Neumann and Dirichlet boundary constraints, b) the smoothness of  
712 complex terrain slope, c) the algorithm assumptions of mass continuity and terrain boundary, and  
713 d) the grid spacing and Gaussian recursive filter setting. Finally, an observational radar analysis is  
714 presented to demonstrate that this new technique can advance scientific analyses in understanding  
715 the impact of orographic forcing on precipitation and wind flow using observational datasets.

716 In this improved SAMURAI technique, the Neumann and Dirichlet boundary conditions are  
717 implemented and treated as pseudo-observations, allowing users to adjust the strength of prescribed  
718 boundary constraints related to surface impermeability and topographic forcings. Our results from  
719 the OSSEs show that the strength of the immersed boundary method constraints can impact the  
720 overall retrieval analysis. The sensitivity test shows that the Dirichlet boundary condition generally  
721 has a greater impact on the retrieval of vertical wind compared to the Neumann boundary condition.  
722 The best analysis is obtained when the boundary constraints are in the same order as the averaged  
723 terrain map slope. Additionally, the smoothness of complex terrain slopes is found to influence  
724 the overall retrieval. A terrain map with excessively steep slopes for a given grid resolution  
725 may produce erroneous results due to the inability to resolve sub-grid scale winds. On the other  
726 hand, a terrain map with shallower slopes can provide a relatively smooth retrieval with a better



700 FIG. 16. Vertical cross sections of (a) reflectivity, (b) wind speed, (c) vertical wind, (d) absolute vertical  
 701 vorticity, and (e) divergence. These cross sections correspond to the white line depicted in Figure 15. The black  
 702 dot represents the Doppler radar observations, while the red dot represents the pseudo observations created based  
 703 on the boundary condition. The black line indicates the topography. The wind vector in (b) illustrates the wind  
 704 direction and magnitude along the cross section.

727 representation of mesoscale features. The algorithm assumptions regarding the mass continuity  
728 and the terrain boundary conditions, especially the Dirichlet condition, are essential for generating  
729 realistic wind retrieval. Neglecting either of these factors can lead to an incorrect representation  
730 of wind retrieval and potential scientific misinterpretation. Considering the terrain boundary  
731 conditions within complex terrain areas is necessary to ensure the reliability and validity of the  
732 wind retrieval process. The grid spacing and Gaussian recursive filter experiment demonstrate that  
733 increasing the Gaussian recursive filter can reduce noise and preserve features with strong signals,  
734 but there is a trade-off of losing some detailed structures. In general, it is recommended to use a  
735 smaller grid spacing than the data spacing with a larger filter length when data points are sufficient.

736 Our results are based on a specific dual-Doppler geometry, and therefore, the exact numerical  
737 errors may differ in other cases. Caution must be taken when configuring the parameters for  
738 optimal analysis retrieval and interpreting the results. In addition, it should be noted that the  
739 beam blockage effect resulting from complex terrain was not considered in this study. The beam  
740 blockage impact is expected to be minimal based on the domain setup and the specific dual-Doppler  
741 geometry used in our analysis, but results may vary in different scenarios or under different terrain  
742 and radar configurations. The analysis of both simulated and real radar observations from Typhoon  
743 Chanthu (2021) demonstrates that the improved retrieval technique can advance scientific analyses,  
744 and highlight the potential of using radar observations in advancing our knowledge of orographic  
745 precipitation dynamics. Future work will involve conducting additional observational case studies  
746 in different regions and weather systems to validate the robustness of the technique and ensure its  
747 effectiveness in different scenarios.

748 *Acknowledgments.* The research was supported by a Taiwan Ministry of Education graduate fel-  
749 lowship, and the National Science Foundation under Awards AGS-1854559, and SI2-LROSE OAC-  
750 1661663 and AGS-2103785. We thank the Central Weather Bureau for providing the ground-based  
751 radar data used for this study. We would also like to thank Wen-Chau Lee, Russ S. Schumacher,  
752 Kristen L. Rasmussen, Steven C. Reising, and three anonymous reviewers for constructive and  
753 helpful comments that improved the paper.

754 *Data availability statement.* The dataset used in this research can be found at a private figshare  
755 repository 10.6084/m9.figshare.21980066, and is available upon request. The SAMURAI code  
756 can be found at <https://github.com/mmbell/samurai>.

## 757 **References**

758 Bell, M. M., M. Dixon, W.-C. Lee, B. Javornik, J. C. DeHart, and T.-Y. Cha, 2021: nsf-lrose/lrose-  
759 elle: lrose-elle stable final release 20210312 (lrose-elle-20210312). *Zenodo*, [https://doi.org/](https://doi.org/10.5281/zenodo.5523312)  
760 [10.5281/zenodo.5523312](https://doi.org/10.5281/zenodo.5523312).

761 Bell, M. M., M. T. Montgomery, and K. A. Emanuel, 2012: Air–sea enthalpy and momentum  
762 exchange at major hurricane wind speeds observed during CBLAST. *Journal of the Atmospheric*  
763 *Sciences*, **69** (11), 3197–3222, <https://doi.org/10.1175/JAS-D-11-0276.1>.

764 Bousquet, O., and M. Chong, 1998: A multiple-Doppler synthesis and continuity adjustment  
765 technique (MUSCAT) to recover wind components from Doppler radar measurements. *Journal*  
766 *of Atmospheric and Oceanic Technology*, **15** (2), 343–359.

767 Cha, T.-Y., 2023: Investigation of the dynamics of tropical cyclone precipitation structure using  
768 radar observations and numerical modeling. *Ph.D. thesis*, Colorado State University.

769 Cha, T.-Y., and M. M. Bell, 2021: Comparison of single-doppler and multiple-Doppler wind  
770 retrievals in Hurricane Matthew (2016). *Atmospheric Measurement Techniques*, **14** (5), 3523–  
771 3539, <https://doi.org/10.5194/amt-14-3523-2021>, URL [https://amt.copernicus.org/articles/14/](https://amt.copernicus.org/articles/14/3523/2021/)  
772 [3523/2021/](https://amt.copernicus.org/articles/14/3523/2021/).

773 Cha, T.-Y., M. M. Bell, W.-C. Lee, and A. J. DesRosiers, 2020: Polygonal  
774 eyewall asymmetries during the rapid intensification of hurricane michael (2018).



775 *Geophysical Research Letters*, **47 (15)**, e2020GL087919, <https://doi.org/https://doi.org/10.1029/2020GL087919>, URL <https://agupubs.onlinelibrary.wiley.com/doi/abs/10.1029/2020GL087919>, e2020GL087919 10.1029/2020GL087919, <https://agupubs.onlinelibrary.wiley.com/doi/pdf/10.1029/2020GL087919>.

779 Chien, F.-C., and H.-C. Kuo, 2011: On the extreme rainfall of typhoon Morakot (2009). *Journal of Geophysical Research: Atmospheres*, **116 (D5)**.

781 Chong, c., M, and Coauthors, 2000: Real-time wind synthesis from Doppler radar observations during the Mesoscale Alpine Programme. *Bulletin of the American Meteorological Society*, **81 (12)**, 2953–2962.

784 Chong, M., and S. Cosma, 2000: A formulation of the continuity equation of MUSCAT for either flat or complex terrain. *Journal of Atmospheric and Oceanic Technology*, **17 (11)**, 1556–1565.

786 Colle, B. A., 2004: Sensitivity of orographic precipitation to changing ambient conditions and terrain geometries: An idealized modeling perspective. *Journal of the atmospheric sciences*, **61 (5)**, 588–606.

789 Collis, S., A. Protat, and K.-S. Chung, 2010: The effect of radial velocity gridding artifacts on variationally retrieved vertical velocities. *Journal of Atmospheric and Oceanic Technology*, **27 (7)**, 1239 – 1246, <https://doi.org/10.1175/2010JTECHA1402.1>, URL [https://journals.ametsoc.org/view/journals/atot/27/7/2010jtecha1402\\_1.xml](https://journals.ametsoc.org/view/journals/atot/27/7/2010jtecha1402_1.xml).

793 Davies-Jones, R. P., 1979: Dual-Doppler radar coverage area as a function of measurement accuracy and spatial resolution. *Journal of Applied Meteorology (1962-1982)*, 1229–1233.

795 del Moral, A., T. M. Weckwerth, T. Rigo, M. M. Bell, and M. C. Llasat, 2020: C-band Dual-Doppler retrievals in complex terrain: Improving the knowledge of severe storm dynamics in Catalonia. *Remote Sensing*, **12 (18)**, <https://doi.org/10.3390/rs12182930>, URL <https://www.mdpi.com/2072-4292/12/18/2930>.

799 Dennis, J. M., A. H. Baker, B. Dobbins, M. M. Bell, J. Sun, Y. Kim, and T.-Y. Cha, 2022: Enabling efficient execution of a variational data assimilation application. *The International Journal of High Performance Computing Applications*, 10943420221119801.

- 802 Foerster, A. M., M. M. Bell, P. A. Harr, and S. C. Jones, 2014: Observations of the eyewall structure  
803 of Typhoon Sinlaku (2008) during the transformation stage of extratropical transition. *Monthly*  
804 *Weather Review*, **142** (9), 3372 – 3392, <https://doi.org/10.1175/MWR-D-13-00313.1>.
- 805 Friedrich, K., and M. Hagen, 2004: Evaluation of wind vectors measured by a bistatic Doppler  
806 radar network. *Journal of Atmospheric and Oceanic Technology*, **21** (12), 1840–1854.
- 807 Gamache, J. F., F. D. Marks, and F. Roux, 1995: Comparison of three airborne Doppler sampling  
808 techniques with airborne in situ wind observations in Hurricane Gustav (1990). *J. Atmos. Oceanic*  
809 *Technol.*, **12** (1), 171 – 181, [https://doi.org/10.1175/1520-0426\(1995\)012<0171:COTADS>2.0.](https://doi.org/10.1175/1520-0426(1995)012<0171:COTADS>2.0.CO;2)  
810 [CO;2](https://doi.org/10.1175/1520-0426(1995)012<0171:COTADS>2.0.CO;2).
- 811 Gao, J., M. Xue, K. Brewster, and K. K. Droegemeier, 2004: A three-dimensional variational data  
812 analysis method with recursive filter for Doppler radars. *Journal of Atmospheric and oceanic*  
813 *technology*, **21** (3), 457–469.
- 814 Gao, J., M. Xue, A. Shapiro, and K. K. Droegemeier, 1999: A variational method for the analysis  
815 of three-dimensional wind fields from two Doppler radars. *Monthly weather review*, **127** (9),  
816 2128–2142.
- 817 Georgis, J., F. Roux, and P. Hildebrand, 2000: Observation of precipitating systems over complex  
818 orography with meteorological Doppler radars: A feasibility study. *Meteorology and Atmo-*  
819 *spheric Physics*, **72** (2), 185–202.
- 820 Hildebrand, P. H., and C. K. Mueller, 1985: Evaluation of meteorological airborne Doppler radar.  
821 Part I: Dual-Doppler analyses of air motions. *J. Atmos. Oceanic Technol.*, **2** (3), 362 – 380,  
822 [https://doi.org/10.1175/1520-0426\(1985\)002<0362:EOMADR>2.0.CO;2](https://doi.org/10.1175/1520-0426(1985)002<0362:EOMADR>2.0.CO;2).
- 823 Hildebrand, P. H., C. A. Walther, C. L. Frush, J. Testud, and F. Baudin, 1994: The EL-  
824 DORA/ASTRAIA airborne Doppler weather radar: goals, design, and first field tests. *Pro-*  
825 *ceedings of the IEEE*, **82** (12), 1873–1890, <https://doi.org/10.1109/5.338076>.
- 826 Hildebrand, P. H., and Coauthors, 1996: The ELDORA/ASTRAIA airborne Doppler weather radar:  
827 High-resolution observations from TOGA COARE. *Bulletin of the American Meteorological*  
828 *Society*, **77** (2), 213–232.

- 829 Houze, R. A., 2012: Orographic effects on precipitating clouds. *Reviews of Geo-*  
830 *physics*, **50** (1), <https://doi.org/https://doi.org/10.1029/2011RG000365>, URL <https://agupubs.onlinelibrary.wiley.com/doi/abs/10.1029/2011RG000365>, <https://agupubs.onlinelibrary.wiley.com/doi/pdf/10.1029/2011RG000365>.
- 833 Kirshbaum, D. J., and D. R. Durran, 2005: Observations and modeling of banded orographic  
834 convection. *Journal of the atmospheric sciences*, **62** (5), 1463–1479.
- 835 Koch, S. E., M. desJardins, and P. J. Kocin, 1983: An interactive Barnes objective map analysis  
836 scheme for use with satellite and conventional data. *J. Appl. Meteor. Climatol.*, **22** (9), 1487 –  
837 1503, [https://doi.org/10.1175/1520-0450\(1983\)022<1487:AIBOMA>2.0.CO;2](https://doi.org/10.1175/1520-0450(1983)022<1487:AIBOMA>2.0.CO;2).
- 838 Liou, Y.-C., S.-F. Chang, and J. Sun, 2012: An application of the immersed boundary method for  
839 recovering the three-dimensional wind fields over complex terrain using multiple-Doppler radar  
840 data. *Monthly weather review*, **140** (5), 1603–1619.
- 841 Liou, Y.-C., and Y.-J. Chang, 2009: A variational multiple-Doppler radar three-dimensional wind  
842 synthesis method and its impacts on thermodynamic retrieval. *Monthly weather review*, **137** (11),  
843 3992–4010.
- 844 Lundquist, K. A., F. K. Chow, and J. K. Lundquist, 2010: An immersed boundary method for the  
845 weather research and forecasting model. *Monthly Weather Review*, **138** (3), 796–817.
- 846 Martinez, J., M. M. Bell, R. F. Rogers, and J. D. Doyle, 2019: Axisymmetric potential vorticity  
847 evolution of Hurricane Patricia (2015). *Journal of the Atmospheric Sciences*, **76** (7), 2043–2063,  
848 <https://doi.org/10.1175/JAS-D-18-0373.1>.
- 849 Matejka, T., and D. L. Bartels, 1998: The accuracy of vertical air velocities from Doppler Radar  
850 Data. *Monthly Weather Review*, **126** (1), 92 – 117, [https://doi.org/10.1175/1520-0493\(1998\)](https://doi.org/10.1175/1520-0493(1998)126<0092:TAOVAV>2.0.CO;2)  
851 [126<0092:TAOVAV>2.0.CO;2](https://doi.org/10.1175/1520-0493(1998)126<0092:TAOVAV>2.0.CO;2).
- 852 Morrison, H., J. A. Curry, and V. I. Khvorostyanov, 2005: A new double-moment microphysics  
853 parameterization for application in cloud and climate models. Part I: Description. *J. Atmos. Sci.*,  
854 **62** (6), 1665 – 1677, <https://doi.org/https://doi.org/10.1175/JAS3446.1>.

- 855 NAKANISHI, M., and H. NIINO, 2009: Development of an improved turbulence closure model  
856 for the atmospheric boundary layer. *Journal of the Meteorological Society of Japan. Ser. II*,  
857 **87 (5)**, 895–912, <https://doi.org/10.2151/jmsj.87.895>.
- 858 North, K. W., M. Oue, P. Kollias, S. E. Giangrande, S. M. Collis, and C. K. Potvin, 2017: Vertical air  
859 motion retrievals in deep convective clouds using the arm scanning radar network in oklahoma  
860 during mc3e. *Atmospheric Measurement Techniques*, **10 (8)**, 2785–2806, <https://doi.org/10.5194/amt-10-2785-2017>, URL <https://amt.copernicus.org/articles/10/2785/2017/>.
- 862 Ooyama, K. V., 1987: Scale-controlled objective analysis. *Mon. Wea. Rev.*, **115 (10)**, 2479 – 2506,  
863 [https://doi.org/10.1175/1520-0493\(1987\)115<2479:SCOA>2.0.CO;2](https://doi.org/10.1175/1520-0493(1987)115<2479:SCOA>2.0.CO;2).
- 864 Ooyama, K. V., 2002: The cubic-spline transform method: Basic definitions and tests in a 1d  
865 single domain. *Mon. Wea. Rev.*, **130 (10)**, 2392 – 2415, [https://doi.org/10.1175/1520-0493\(2002\)](https://doi.org/10.1175/1520-0493(2002)130<2392:TCSTMB>2.0.CO;2)  
866 [130<2392:TCSTMB>2.0.CO;2](https://doi.org/10.1175/1520-0493(2002)130<2392:TCSTMB>2.0.CO;2).
- 867 Oue, M., P. Kollias, A. Shapiro, A. Tatarevic, and T. Matsui, 2019: Investigation of obser-  
868 vational error sources in multi-Doppler-radar three-dimensional variational vertical air mo-  
869 tion retrievals. *Atmospheric Measurement Techniques*, **12 (3)**, 1999–2018, [https://doi.org/](https://doi.org/10.5194/amt-12-1999-2019)  
870 [10.5194/amt-12-1999-2019](https://doi.org/10.5194/amt-12-1999-2019), URL <https://amt.copernicus.org/articles/12/1999/2019/>.
- 871 Oue, M., A. Tatarevic, P. Kollias, D. Wang, K. Yu, and A. M. Vogelmann, 2020: The cloud-  
872 resolving model Radar SIMulator (CR-SIM) version 3.3: description and applications of a virtual  
873 observatory. *Geoscientific Model Development*, **13 (4)**, 1975–1998, [https://doi.org/10.5194/](https://doi.org/10.5194/gmd-13-1975-2020)  
874 [gmd-13-1975-2020](https://doi.org/10.5194/gmd-13-1975-2020), URL <https://gmd.copernicus.org/articles/13/1975/2020/>.
- 875 Potvin, C. K., D. Betten, L. J. Wicker, K. L. Elmore, and M. I. Biggerstaff, 2012a: 3DVAR versus  
876 traditional dual-Doppler wind retrievals of a simulated supercell thunderstorm. *Mon. Wea. Rev.*,  
877 **140 (11)**, 3487 – 3494, [https://doi.org/https://doi.org/10.1175/MWR-D-12-00063.1](https://doi.org/10.1175/MWR-D-12-00063.1), URL [https://journals.](https://journals.ametsoc.org/view/journals/mwre/140/11/mwr-d-12-00063.1.xml)  
878 [ametsoc.org/view/journals/mwre/140/11/mwr-d-12-00063.1.xml](https://journals.ametsoc.org/view/journals/mwre/140/11/mwr-d-12-00063.1.xml).
- 879 Potvin, C. K., L. J. Wicker, and A. Shapiro, 2012b: Assessing errors in vari-  
880 ational Dual-Doppler wind syntheses of supercell thunderstorms observed by storm-  
881 scale mobile radars. *Journal of Atmospheric and Oceanic Technology*, **29 (8)**, 1009 –

882 1025, <https://doi.org/10.1175/JTECH-D-11-00177.1>, URL [https://journals.ametsoc.org/view/journals/atot/29/8/jtech-d-11-00177\\_1.xml](https://journals.ametsoc.org/view/journals/atot/29/8/jtech-d-11-00177_1.xml).

884 Protat, A., and I. Zawadzki, 1999: A variational method for real-time retrieval of three-dimensional  
885 wind field from multiple-Doppler bistatic radar network data. *Journal of Atmospheric and*  
886 *Oceanic Technology*, **16** (4), 432–449.

887 Purser, R. J., W.-S. Wu, D. F. Parrish, and N. M. Roberts, 2003: Numerical aspects of the  
888 application of recursive filters to variational statistical analysis. Part I: Spatially Homoge-  
889 neous and Isotropic Gaussian Covariances. *Monthly Weather Review*, **131** (8), 1524 – 1535,  
890 [https://doi.org/10.1175//1520-0493\(2003\)131<1524:NAOTAO>2.0.CO;2](https://doi.org/10.1175//1520-0493(2003)131<1524:NAOTAO>2.0.CO;2), URL [https://journals.ametsoc.org/view/journals/mwre/131/8/\\_1520-0493\\_2003\\_131\\_1524\\_naotao\\_2.0.co\\_2.xml](https://journals.ametsoc.org/view/journals/mwre/131/8/_1520-0493_2003_131_1524_naotao_2.0.co_2.xml).

892 Ray, P. S., J. J. Stephens, and K. W. Johnson, 1979: Multiple-doppler radar network de-  
893 sign. *Journal of Applied Meteorology and Climatology*, **18** (5), 706 – 710, [https://doi.org/10.1175/1520-0450\(1979\)018<0706:MDRND>2.0.CO;2](https://doi.org/10.1175/1520-0450(1979)018<0706:MDRND>2.0.CO;2), URL [https://journals.ametsoc.org/view/journals/apme/18/5/1520-0450\\_1979\\_018\\_0706\\_mdrnd\\_2\\_0\\_co\\_2.xml](https://journals.ametsoc.org/view/journals/apme/18/5/1520-0450_1979_018_0706_mdrnd_2_0_co_2.xml).

896 Ray, P. S., C. L. Ziegler, W. Bumgarner, and R. J. Serafin, 1980: Single- and multiple-Doppler  
897 radar observations of tornadic storms. *Monthly Weather Review*, **108** (10), 1607–1625.

898 Singh, J., and Coauthors, 2021: Effects of spatial resolution on WRF v3.8.1 simulated meteorology  
899 over the central Himalaya. *Geoscientific Model Development*, **14** (3), 1427–1443, <https://doi.org/10.5194/gmd-14-1427-2021>, URL <https://gmd.copernicus.org/articles/14/1427/2021/>.

901 Skamarock, W. C., J. B. Klemp, J. Dudhia, D. O. Gill, Z. Liu, J. Berner, and X.-y.  
902 Huang, 2021: A description of the advanced research WRF model version 4.3. Tech. Rep.  
903 No. NCAR/TN-556+STR, University Corporation for Atmospheric Research. <https://doi.org/10.5065/1dfh-6p97>.

905 Smith, R. B., and I. Barstad, 2004: A linear theory of orographic precipitation. *Journal of the At-*  
906 *mospheric Sciences*, **61** (12), 1377 – 1391, [https://doi.org/10.1175/1520-0469\(2004\)061<1377:ALTOOP>2.0.CO;2](https://doi.org/10.1175/1520-0469(2004)061<1377:ALTOOP>2.0.CO;2), URL [https://journals.ametsoc.org/view/journals/atasc/61/12/1520-0469\\_2004\\_061\\_1377\\_altoop\\_2.0.co\\_2.xml](https://journals.ametsoc.org/view/journals/atasc/61/12/1520-0469_2004_061_1377_altoop_2.0.co_2.xml).

909 Spacesystems, N., and U. A. S. Team, 2019: ASTER Global Digital Elevation Model V003  
910 [Data set]. NASA EOSDIS Land Processes DAAC. *Accessed 2022-10-24 from*, [https://doi.org/  
911 https://doi.org/10.5067/ASTER/ASTGTM.003](https://doi.org/https://doi.org/10.5067/ASTER/ASTGTM.003).

912 Steiner, M., 1991: A new relationship between mean Doppler velocity and differential reflec-  
913 tivity. *Journal of Atmospheric and Oceanic Technology*, **8 (3)**, 430 – 443, [https://doi.org/  
914 10.1175/1520-0426\(1991\)008\(0430:ANRBMD\)2.0.CO;2](https://doi.org/10.1175/1520-0426(1991)008(0430:ANRBMD)2.0.CO;2), URL [https://journals.ametsoc.org/  
915 view/journals/atot/8/3/1520-0426\\_1991\\_008\\_0430\\_anrbmd\\_2\\_0\\_co\\_2.xml](https://journals.ametsoc.org/view/journals/atot/8/3/1520-0426_1991_008_0430_anrbmd_2_0_co_2.xml).

916 Tseng, Y.-H., and J. H. Ferziger, 2003: A ghost-cell immersed boundary method for flow in  
917 complex geometry. *Journal of computational physics*, **192 (2)**, 593–623.

918 Zipser, E. J., D. J. Cecil, C. Liu, S. W. Nesbitt, and D. P. Yorty, 2006: Where are  
919 the most intense thunderstorms on earth? *Bull. Amer. Meteor. Soc.*, **87 (8)**, 1057  
920 – 1072, <https://doi.org/10.1175/BAMS-87-8-1057>, URL [https://journals.ametsoc.org/view/  
921 journals/bams/87/8/bams-87-8-1057.xml](https://journals.ametsoc.org/view/journals/bams/87/8/bams-87-8-1057.xml).